

# Quantum Approximate Optimization Algorithm: Performance, Mechanism, and Implementation on Near-Term Devices

Leo Zhou,<sup>1,\*</sup> Sheng-Tao Wang,<sup>1,†</sup> Soonwon Choi,<sup>1,2</sup> Hannes Pichler,<sup>3,1</sup> and Mikhail D. Lukin<sup>1</sup>

<sup>1</sup>*Department of Physics, Harvard University, Cambridge, MA 02138, USA*

<sup>2</sup>*Department of Physics, University of California Berkeley, Berkeley, CA 94720, USA*

<sup>3</sup>*ITAMP, Harvard-Smithsonian Center for Astrophysics, Cambridge, MA 02138, USA*

(Dated: May 28, 2022)

The Quantum Approximate Optimization Algorithm (QAOA) is a hybrid quantum-classical variational algorithm designed to tackle combinatorial optimization problems. Despite its promise for near-term quantum applications, not much is currently understood about QAOA’s performance beyond its lowest-depth variant. An essential but missing ingredient for understanding and deploying QAOA is a constructive approach to carry out the outer-loop classical optimization. We provide an in-depth study of the performance of QAOA on MaxCut problems by developing an efficient parameter-optimization procedure and revealing its ability to exploit non-adiabatic operations. Building on observed patterns in optimal parameters, we propose heuristic optimization strategies that find quasi-optimal parameters in  $O(\text{poly}(p))$  time without the  $2^{O(p)}$  resources required by brute-force approaches. We then benchmark QAOA and compare it with quantum annealing, especially on difficult instances where adiabatic quantum annealing fails due to small spectral gaps. The comparison reveals that QAOA can learn via optimization to utilize non-adiabatic mechanisms to circumvent the challenges associated with vanishing spectral gaps. Finally, we provide a realistic resource analysis on the experimental implementation of QAOA. When quantum fluctuations in measurements are accounted for, we illustrate that optimization will be important only for problem sizes beyond numerical simulations, but accessible on near-term devices. We propose a feasible implementation of large MaxCut problems with a few hundred vertices in a system of 2D neutral atoms, reaching the regime to challenge the best classical algorithms.

## I. INTRODUCTION

As quantum computing systems develop, there is a growing interest in finding useful applications of near-term quantum machines [1]. In the near future, however, the number of reliable quantum gates will be limited by noise and decoherence. As such, hybrid quantum-classical algorithms [2–4] have been proposed to make the best of available quantum resources and integrate them with classical routines. The Quantum Approximate Optimization Algorithm (QAOA) [2] and the Variational Quantum Eigensolver [3] are such algorithms put forward to address classical combinatorial optimization and quantum chemistry problems, respectively. Proof-of-principle experiments running these algorithms have already been demonstrated in the lab [5–7].

In these hybrid algorithms, a quantum processor prepares a quantum state according to a set of variational parameters. Using measurement outputs, the parameters are then optimized by a classical computer and fed back to the quantum machine in a closed loop. In QAOA, the state is prepared by a  $p$ -level circuit specified by  $2p$  variational parameters. Even at the lowest circuit depth ( $p = 1$ ), QAOA has non-trivial provable performance guarantees [2, 8] and is not efficiently simulatable by classical computers [9]. It is thus an appeal

ing algorithm to explore quantum speedups on near-term quantum machines. However, very little is known about QAOA beyond the lowest depth. One major hurdle lies in the difficulty to efficiently optimize in the non-convex, high-dimensional parameter landscape. Without constructive approaches to perform the parameter optimization, any potential advantages of the hybrid algorithms could be lost [10]. Furthermore, although QAOA is known to succeed in the  $p \rightarrow \infty$  limit due to its ability to approximate adiabatic quantum annealing (i.e., the adiabatic algorithm) [2], its performance when  $1 < p \ll \infty$  is largely unexplored.

In this work, we contribute, in three major aspects, to the understanding and applicability of QAOA on near-term devices, with a focus on MaxCut problems. First, we develop heuristic strategies to efficiently optimize QAOA variational parameters. These strategies are found, via extensive benchmarking, to be quasi-optimal in the sense that they usually produce known global optima, and generically require  $2^{O(p)}$  brute-force optimization runs to surpass. Secondly, we benchmark the performance of QAOA and compare it with quantum annealing. On difficult graph instances where the minimum spectral gap is very small, QAOA is found to outperform adiabatic quantum annealing by multiple orders of magnitude in computation time. Lastly, we provide a detailed resource analysis on the experimental implementation of QAOA with near-term quantum devices. Taking into account of quantum fluctuations in projective measurements, we argue that optimization will play a role only for much larger problem sizes than numerically accessible ones. We

\* [leozhou@g.harvard.edu](mailto:leozhou@g.harvard.edu)

† [shengtaowst@fas.harvard.edu](mailto:shengtaowst@fas.harvard.edu);

L.Z. and S.-T.W. contributed equally to this work.

also propose a 2D physical implementation of QAOA on MaxCut with a few hundred Rydberg-interacting atoms, which can be put to the test against the best classical algorithm for potential quantum advantages.

Our main results can be summarized as follows. By performing extensive brute-force searches, we discover persistent patterns in the optimal parameters. Based on the observed patterns, we develop efficient optimization strategies, at a cost scaling polynomially in  $p$  in stark contrast to the  $2^{O(p)}$  resource required by brute-force approaches. We also propose a new parametrization of QAOA that can significantly simplify optimization by reducing the dimension of the search space. Using our heuristic strategy, we benchmark the performance of QAOA on many instances of MaxCut up to  $N \leq 22$  vertices and level  $p \leq 50$ . Comparing QAOA with quantum annealing, we find the former can learn via optimization to utilize diabatic mechanisms [11–14] and overcome the challenges faced by adiabatic quantum annealing due to very small spectral gaps. Considering realistic experimental implementations, we also study the effects of quantum “projection noise” in measurement: we find that, for numerically accessible problem sizes, QAOA can often obtain the solution among measurement outputs before the best variational parameters are found. Parameter optimization will be more useful at large system sizes (a few hundred vertices), as one expects the probability of finding the solution from projective measurements to decrease exponentially. At such system sizes, we analyze a procedure to make graphs more experimentally realizable by reducing the required range of qubit interactions via vertex renumbering. Finally, we discuss a specific implementation using neutral atoms interacting via Rydberg excitations [15, 16], where a 2D implementation with a few hundred atoms appears feasible on a near-term device.

The rest of the paper is organized in the following order: In Sec. II, we review QAOA and the MaxCut problem. In Sec. III, we describe some patterns found for QAOA optimal parameters and introduce a class of heuristic optimization strategies based on the observed patterns. We benchmark our heuristic strategies and study the performance of QAOA on typical MaxCut graph instances in Sec. IV. We then, in Sec. V, compare QAOA with quantum annealing, shedding light on the non-adiabatic mechanism of QAOA. Lastly, we discuss considerations for experimental implementations for large problem sizes in Sec. VI.

## II. QUANTUM APPROXIMATE OPTIMIZATION ALGORITHM

Many interesting real-world problems can be framed as combinatorial optimization problems [17, 18]. These are problems defined on  $N$ -bit binary strings  $\mathbf{z} = z_1 \cdots z_N$ , where the goal is to determine a string that maximizes a given classical objective function  $C(\mathbf{z}) : \{+1, -1\}^N \mapsto$

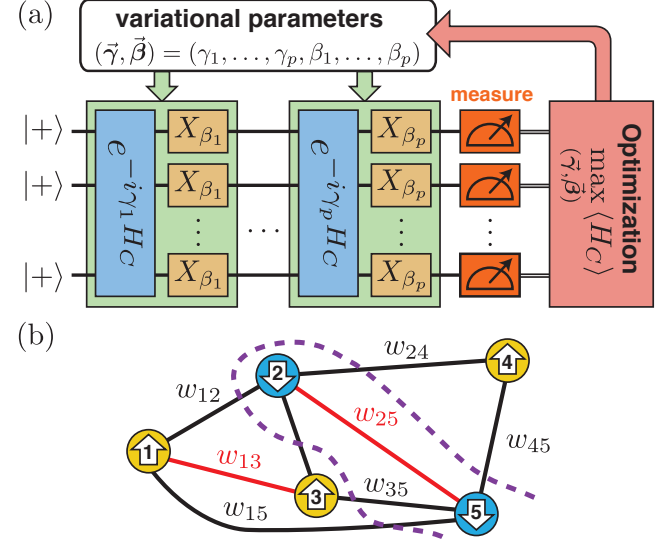


FIG. 1. (a) Schematic of a  $p$ -level Quantum Approximation Optimization Algorithm [2]. A quantum circuit takes input  $|+\rangle^{\otimes N}$  and alternately applies  $e^{-i\gamma_i H_C}$  and  $X_{\beta_i} = e^{-i\beta_i \sigma^x}$ , and the final state is measured to obtain expectation value with respect to the objective function  $H_C$ . This is fed to a (classical) optimizer to find the best parameters  $(\vec{\gamma}, \vec{\beta})$  that maximizes  $\langle H_C \rangle$ . (b) An example of a MaxCut problem on a 5-vertex graph, where one seeks an assignment of spin variables on the vertices such that the sum of edge weights between anti-aligned spins is maximized (black edges).

$\mathbb{R}_{\geq 0}$ . An approximate optimization algorithm aims to find a string  $\mathbf{z}$  that achieves a desired approximation ratio

$$\frac{C(\mathbf{z})}{C_{\max}} \geq r^*, \quad (1)$$

where  $C_{\max} = \max_{\mathbf{z}} C(\mathbf{z})$ .

The Quantum Approximate Optimization Algorithm (QAOA) is a quantum algorithm recently introduced to tackle these combinatorial optimization problems [2]. To encode the problem, the classical objective function can be converted into a quantum problem Hamiltonian by promoting each binary variable  $z_i$  into a quantum spin  $\sigma_i^z$ :

$$H_C = C(\sigma_1^z, \sigma_2^z, \dots, \sigma_N^z). \quad (2)$$

For  $p$ -level QAOA, which is visualized in Fig. 1(a), we initialize the quantum processor in the state  $|+\rangle^{\otimes N}$ , and then apply the problem Hamiltonian  $H_C$  and a mixing Hamiltonian  $H_B = \sum_{j=1}^N \sigma_j^x$  alternately with controlled durations to generate a variational wavefunction

$$|\psi_p(\vec{\gamma}, \vec{\beta})\rangle = e^{-i\beta_p H_B} e^{-i\gamma_p H_C} \cdots e^{-i\beta_1 H_B} e^{-i\gamma_1 H_C} |+\rangle^{\otimes N}, \quad (3)$$

which is parameterized by  $2p$  parameters  $\gamma_i$  and  $\beta_i$  ( $i = 1, 2, \dots, p$ ). We then determine the expectation value  $H_C$

in this variational state

$$F_p(\vec{\gamma}, \vec{\beta}) = \langle \psi_p(\vec{\gamma}, \vec{\beta}) | H_C | \psi_p(\vec{\gamma}, \vec{\beta}) \rangle, \quad (4)$$

which is done by repeated measurements of the quantum system in the computational basis. A classical computer is used to search for the optimal parameters  $(\vec{\gamma}^*, \vec{\beta}^*)$  so as to maximize  $F_p(\vec{\gamma}, \vec{\beta})$ ,

$$(\vec{\gamma}^*, \vec{\beta}^*) = \arg \max_{\vec{\gamma}, \vec{\beta}} F_p(\vec{\gamma}, \vec{\beta}). \quad (5)$$

A figure of merit for benchmarking the performance of QAOA is the approximation ratio

$$r = \frac{F_p(\vec{\gamma}^*, \vec{\beta}^*)}{C_{\max}}. \quad (6)$$

The framework of QAOA can be applied to general combinatorial optimization problems. Here, we focus on its application to an archetypical problem called MaxCut, which is a combinatorial problem whose approximate optimization beyond a minimum ratio  $r^*$  is NP-hard [19, 20]. The MaxCut problem, visualized in Fig. 1(b), is defined for any input graph  $G = (V, E)$ . Here,  $V = \{1, 2, \dots, N\}$  denotes the set of vertices and  $E = \{\langle i, j \rangle, w_{ij}\}$  is the set of edges, where  $w_{ij} \in \mathbb{R}_{\geq 0}$  is the weight of the edge  $\langle i, j \rangle$  connecting vertices  $i$  and  $j$ . The goal of MaxCut is to maximize the following objective function

$$H_C = \sum_{\langle i, j \rangle} \frac{w_{ij}}{2} (1 - \sigma_i^z \sigma_j^z), \quad (7)$$

where an edge  $\langle i, j \rangle$  contributes with weight  $w_{ij}$  if and only if spins  $\sigma_i^z$  and  $\sigma_j^z$  are anti-aligned.

For simplicity, we restrict our attention to MaxCut on  $d$ -regular graphs, where every vertex is connected to exactly  $d$  other vertices. We study two classes of graphs: the first is unweighted  $d$ -regular graphs (u2R), where all edges have equal weights  $w_{ij} = 1$ ; the second is weighted  $d$ -regular graphs (w2R), where the weights  $w_{ij}$  are chosen uniformly at random from  $[0, 1]$ . It is NP-hard to design an algorithm that guarantees a minimum approximation ratio of  $r^* \geq 16/17$  for MaxCut on all graphs [19], or  $r^* \geq 331/332$  when restricted to u3R graphs [20]. The current record for approximation ratio guarantee on generic graphs belongs to Goemans-Williamson [21], which achieves  $r^* \approx 0.87856$  using semidefinite programming. This lower bound can be raised to  $r^* \approx 0.9326$  when restricted to u3R graphs [22]. Farhi *et al.* [2] were able to prove that QAOA at level  $p = 1$  achieves  $r^* \geq 0.6924$  for u3R graphs, using the fact that  $F_p$  can be written as a sum of quasi-local terms, each corresponding to a subgraph involving edges at most  $p$  steps away from a given edge. However, this approach to bound  $r^*$  quickly becomes intractable since the locality of each term (i.e., size of each subgraph) grows exponentially in  $p$ , as does the number of subgraph types

involved.

QAOA is believed to be a promising algorithm for multiple reasons [2, 8, 9, 23–28]. As mentioned above, for certain cases one can prove a guaranteed minimum approximation ratio when  $p = 1$  [2, 8]. Additionally, under reasonable complexity-theoretic assumptions, QAOA cannot be efficiently simulated by any classical computer even when  $p = 1$ , making it a suitable candidate algorithm to establish the so-called “quantum supremacy” [9]. It has also been argued that the square-pulse (“bang-bang”) ansatz of dynamical evolution, of which QAOA is an example, is optimal given a fixed quantum computation time [25]. In general, the performance of QAOA can only improve with increasing  $p$ , achieving  $r \rightarrow 1$  when  $p \rightarrow \infty$  since it can approximate adiabatic quantum annealing via Trotterization; this monotonicity makes it more attractive than quantum annealing whose performance may decrease with increased run time [11].

While QAOA has a simple description, not much is currently understood beyond  $p = 1$ . For the toy example of MaxCut on u2R graphs, i.e. 1D antiferromagnetic rings, it was conjectured that QAOA yields  $r \geq (2p+1)/(2p+2)$  based on numerical evidence [2, 23][29]. In another example of Grover’s unstructured search problem among  $n$  items, QAOA is shown to be able to find the target state with  $p = \Theta(\sqrt{n})$ , achieving the optimal query complexity within a constant factor [27]. For more general problems, Farhi *et al.* [2] proposed a simple brute-force approach by discretizing each parameter into  $O(\text{poly}(N))$  grid points; this, however, requires examining  $N^{O(p)}$  possibilities at level  $p$ , which quickly becomes impractical as  $p$  grows. An efficient optimization of QAOA parameters and understanding of the algorithm for  $1 \ll p < \infty$  remain outstanding problems. We aim to tackle these problems in the present work.

### III. OPTIMIZING VARIATIONAL PARAMETERS

In this section, we address the issue of parameter optimization in QAOA, since brute-force approaches to search for the best parameters generally become exponentially difficult as level  $p$  increases. We mostly restrict our discussion to randomly generated instances of u3R and w3R graphs. Similar results are found for u4R and w4R graphs, as well as complete graphs with random weights (or, equivalently, the Sherrington-Kirkpatrick spin glass problem). We utilize patterns in the optimal parameters to develop heuristic strategies that can efficiently find quasi-optimal solutions in  $O(\text{poly}(p))$  time.

#### A. Patterns in optimal parameters

Before searching for patterns in optimal QAOA parameters, it is useful to eliminate degeneracies in the

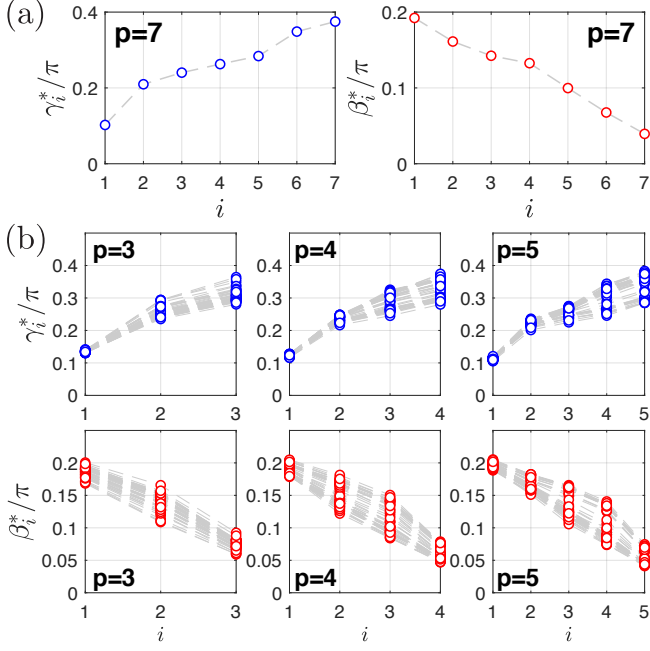


FIG. 2. (a) Optimal QAOA parameters  $(\vec{\gamma}^*, \vec{\beta}^*)$  for an example instance of MaxCut on a 16-vertex unweighted 3-regular (u3R) graph at level  $p = 7$ . (b) The parameter pattern visualized by plotting the optimal parameters of 40 instances of 16-vertex u3R graphs, for  $3 \leq p \leq 5$ . Each dashed line connects parameters for one particular graph instance. For each instance and each  $p$ , we use the classical BFGS optimization algorithm [30] from  $10^4$  random seeds (starting points), and keep the best parameters.

parameter space due to symmetries. Generally, QAOA has a time-reversal symmetry,  $F_p(\vec{\gamma}, \vec{\beta}) = F_p(-\vec{\gamma}, -\vec{\beta})$ , since both  $H_B$  and  $H_C$  are real-valued. For QAOA applied to MaxCut, there is an additional  $\mathbb{Z}_2$  symmetry, as  $e^{-i(\pi/2)H_B} \equiv (\sigma^x)^{\otimes N}$  commutes through the circuit. Furthermore, the structure of the MaxCut problem on  $udR$  graphs creates redundancy since  $e^{-i\pi H_C} = \mathbb{1}$  if  $d$  is even, and  $(\sigma^z)^{\otimes N}$  if  $d$  is odd. These symmetries allow us to restrict  $\beta_i \in [-\frac{\pi}{4}, \frac{\pi}{4}]$  in general, and  $\gamma_i \in [-\frac{\pi}{2}, \frac{\pi}{2}]$  for  $udR$  graphs.

We start by numerically investigating the optimal QAOA parameters for MaxCut on random u3R and w3R graphs with vertex number  $8 \leq N \leq 22$ , using a brute-force approach. For each graph instance and a given level  $p$ , we choose a random starting point (seed) in the parameter space [31] and use a commonly used, gradient-based optimization algorithm known as BFGS [30] to find a local optimum  $(\vec{\gamma}^L, \vec{\beta}^L)$ . This local optimization is repeated with sufficiently many different seeds to find the global optimum  $(\vec{\gamma}^*, \vec{\beta}^*)$  [32]. We then reduce the degeneracies of the optimal parameters  $(\vec{\gamma}^*, \vec{\beta}^*)$  using the aforementioned symmetries. In all cases examined, we find that the global optimum is non-degenerate up to these symmetries.

After performing the above numerical experiment for

100 random u3R and w3R graphs with various vertex number  $N$ , we discover some patterns in the optimal parameters  $(\vec{\gamma}^*, \vec{\beta}^*)$ . Generically, the optimal  $\gamma_i^*$  tends to increase smoothly with  $i = 1, 2, \dots, p$ , while  $\beta_i^*$  tends to decrease smoothly, as shown for the example instance in Fig. 2(a). In Fig. 2(b), we illustrate the pattern by simultaneously plotting the optimal parameters for 40 instances of 16-vertex u3R graphs for  $3 \leq p \leq 5$ . Similar patterns are found for w3R graphs, which we elaborate in Appendix A. Furthermore, for a given class of graphs, the optimal parameters are observed to roughly occupy the same range of values as  $p$  is varied. This demonstrates a clear pattern in the optimal QAOA parameters that we can exploit in the optimization, as we show later in Sec. III B. Similar patterns are found for parameters up to  $p \lesssim 15$ , if the number of random seeds is increased accordingly.

We give two remarks here: First, we note that surprisingly, even at small depth, this parameter pattern is reminiscent of adiabatic quantum annealing where  $H_C$  is gradually turned on while  $H_B$  is gradually turned off. However, we will demonstrate in Sec. V that the mechanism of QAOA goes beyond the adiabatic principle. Secondly, we note that these optimal parameters have a small spread over many different instances. This is because the objective function  $F_p(\vec{\gamma}, \vec{\beta})$  is a sum of terms corresponding to subgraphs involving vertices that are distance  $\leq p$  away from every edge. At small  $p$ , there are only a few relevant subgraph types that enter into  $F_p$  and effectively determine the optimal parameters. As  $N \rightarrow \infty$  and at a fixed finite  $p$ , we expect the probability of a relevant subgraph type appearing in a random graph to approach a fixed fraction. This implies that the distribution of optimal parameters  $(\vec{\gamma}^*, \vec{\beta}^*)$  should converge to a fixed set of values in this limit.

## B. Heuristic optimization strategy for large $p$

The optimal parameter patterns observed above indicate that generically, there is a slowly varying continuous curve that underlies the parameters  $\gamma_i^*$  and  $\beta_i^*$ . Moreover, this curve changes only slightly from level  $p$  to  $p+1$ . Based on these observations, we propose a new parameterization of QAOA, as well as a heuristic optimization strategy that we call FOURIER. The key idea behind the heuristic strategy is to use information from the optimal parameters at level  $p$  to help optimization at level  $p+1$  by producing good starting points. We give a high-level overview of the strategy in this section, while deferring the details of its implementation to Appendix B. While this heuristic is not guaranteed to find the global optimum of QAOA parameters, we show that in Sec. IV A, it can produce, in  $O(\text{poly}(p))$  time, quasi-optima that require  $2^{O(p)}$  number of brute-force runs to surpass. Consequently, this allows us to study the performance and mechanism of QAOA beyond  $p = 1$ .

We begin by proposing a new parameterization of

QAOA based on the observation that the optimal QAOA parameters  $\gamma_i^*$  and  $\beta_i^*$  appear to be smooth functions of their index  $i$ . This inspires an alternative representation of the QAOA parameters using Fourier-related transforms of real numbers, which allow us to reduce the number of necessary parameters. Instead of using the  $2p$  parameters  $(\vec{\gamma}, \vec{\beta}) \in \mathbb{R}^{2p}$ , we switch to  $2q$  parameters  $(\vec{u}, \vec{v}) \in \mathbb{R}^{2q}$ , where the individual elements  $\gamma_i$  and  $\beta_i$  are written as functions of  $(\vec{u}, \vec{v})$  through the following transformation:

$$\gamma_i = \sum_{k=1}^q u_k \sin \left[ \left( k - \frac{1}{2} \right) \left( i - \frac{1}{2} \right) \frac{\pi}{p} \right], \quad (8)$$

$$\beta_i = \sum_{k=1}^q v_k \cos \left[ \left( k - \frac{1}{2} \right) \left( i - \frac{1}{2} \right) \frac{\pi}{p} \right]. \quad (9)$$

These transformations are known as Discrete Sine/Cosine Transform, where  $u_k$  and  $v_k$  can be interpreted as the amplitude of  $k$ -th frequency component for  $\vec{\gamma}$  and  $\vec{\beta}$ , respectively. Note that when  $q \geq p$ , this new parametrization is capable of describing all possible QAOA protocols at level  $p$ .

Our FOURIER strategy works by starting with level  $p = 1$ , optimize, and then use the optimum at level  $p$  to determine a good starting point for level  $p + 1$ . The starting points are generated by simply re-using the optimized amplitudes  $(\vec{u}^*, \vec{v}^*)$  of frequency components from level  $p$  for level  $p + 1$ . We propose several variants of this strategy for optimizing  $p$ -level QAOA: they are called FOURIER $[q, R]$ , characterized by two integer parameters  $q$  and  $R$ . The first integer  $q$  labels the maximum frequency component we allow in the parameters  $(\vec{u}, \vec{v})$ . If  $q = p$ , the full power of  $p$ -level QAOA can be utilized. However, the smoothness of the optimal parameters  $(\vec{\gamma}, \vec{\beta})$  implies that only the low-frequency components are important. Thus, we can also consider the case where  $q$  is a fixed constant independent of  $p$ , so the number of parameters is bounded even as the QAOA circuit depth increases. The second integer  $R$  is the number of controlled random perturbations we add to the parameters so that we can sometimes escape a local optimum towards a better one. More details on different variants of FOURIER strategies and their comparison are described in Appendix B. For the results shown in the rest of the paper, we use the FOURIER $[q, R]$  strategy with  $q = p$  and  $R = 10$  unless otherwise stated.

#### IV. PERFORMANCE OF HEURISTICALLY OPTIMIZED QAOA

##### A. Comparison between our heuristics and brute-force

Let us first compare the performance of our heuristic strategies to the brute-force approach. In Fig. 3(a), we show the result for an example instance of 16-vertex

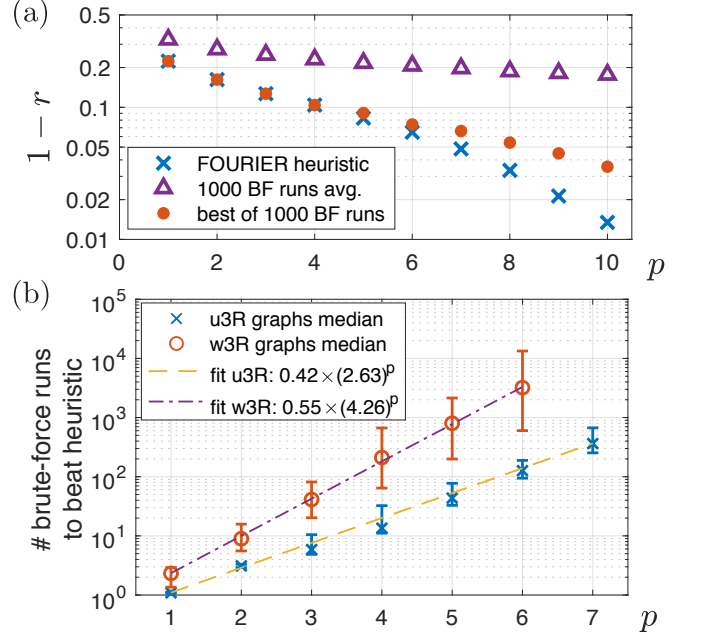


FIG. 3. (a) Comparison between our FOURIER heuristic and the brute-force (BF) approach for optimizing QAOA, on an example instance of 16-vertex w4R graph. The figure of merit  $1 - r$ , where  $r$  is the approximation ratio, is plotted as a function of QAOA level  $p$  on a log-linear scale. The brute-force points are obtained by optimizing from 1000 randomly generated starting points, averaged over 10 such realizations. (b) The median number of brute-force runs needed to obtain an approximation ratio as good as our FOURIER heuristic, for 40 instances of 16-vertex u3R and w3R graphs. A log-linear scale is used, and exponential curves are fitted to the results. Error bars are 5th and 95th percentiles.

w4R graph. At low  $p$ , our FOURIER heuristic strategies perform just as well as the best out of 1000 brute-force runs—both are able to find the global optimum. The average performance of the brute-force strategy, on the other hand, is much worse than our heuristics. This indicates that the QAOA parameter landscape is highly non-convex and filled with low-quality, non-degenerate local optima. When  $p \geq 5$ , our heuristic optimization outperforms the best brute-force run. To estimate the number of brute-force runs needed to find an optimum with the same or better approximation ratio as our FOURIER heuristics, we perform brute-force optimization on 40 instances of 16-vertex u3R and w3R graphs with up to 40000 runs. In Fig. 3(b), the median number of brute-force runs needed to beat our heuristic is shown to scale exponentially with  $p$ . Hence, our heuristics offer a dramatic improvement in the resource required to find good parameters for QAOA; and as we have verified with an excessive number of brute-force runs, the heuristics often find the global optima.

We remark that although we mostly used gradient-based methods (BFGS) in our numerical simulations, non-gradient based approaches, such as the Nelder-

Mead [33] method, work equally well with our heuristic strategies. The choice to use gradient-based optimization is mainly motivated by the simulation speed. Later in Sec. VI, we account for the measurement costs in estimating the gradient using a finite-difference method, and perform a full Monte-Carlo simulation of the entire QAOA algorithm, including quantum fluctuations in the determination of  $F_p$ .

## B. Performance of QAOA on typical instances

With our heuristic optimization strategies in hand, we study the performance of intermediate  $p$ -level QAOA on many graph instances. We consider many randomly generated instances u3R and w3R graphs with vertex number  $8 \leq N \leq 22$ , and use our FOURIER strategy to find optimal QAOA parameters for level  $p \leq 20$ . In the following discussion, we use the fractional error  $1 - r$  to assess the performance of QAOA.

We first examine the case of unweighted graphs, specifically u3R graphs. In Fig. 4(a), we plot the fractional error  $1 - r$  as a function of QAOA's level  $p$ . Here, we see that, on average,  $1 - r \propto e^{-p/p_0}$  appears to decay exponentially with  $p$ . Note that since the instances studied are u3R graphs with system size  $N \leq 22$ , where  $C_{\max} \leq |E| \leq 33$ , we have essentially prepared the MaxCut state whenever the fractional error goes below  $\sim 10^{-2}$ . This good performance can be understood by interpreting QAOA as Trotterized quantum annealing, especially when the optimized parameters are of the pattern seen in Fig. 2, where one initializes in the ground state of  $-H_B$  and evolve with  $H_B$  (and  $H_C$ ) with smoothly decreasing (and increasing) durations. The equivalent total annealing time  $T$  is approximately proportional to the level  $p$ , since the individual parameters  $\gamma_i, \beta_i = O(1)$  and correspond to the evolution times under  $H_C$  and  $H_B$ . If  $T$  is much longer than  $1/\Delta_{\min}^2$ , where  $\Delta_{\min}$  is the minimum spectral gap, quantum annealing will be able to find the exact solution to MaxCut (ground state of  $-H_C$ ) by the adiabatic theorem [14], and achieve exponentially small fractional error as predicted by Landau-Zener [34]. Numerically, we find that the minimum gaps of these u3R instances when running quantum annealing are on the order of  $\Delta_{\min} \gtrsim 0.2$ . It is thus not surprising that QAOA achieves exponentially small fractional error on average, since it is able to prepare the ground state of  $-H_C$  through the adiabatic mechanism for these large-gap instances. Nevertheless, as we will see in the following section, this exponential behavior breaks down for hard instances, where the gap is small.

Let us now turn to the case of w3R graphs. As shown in Fig. 4(b), the fractional error appears to scale as  $1 - r \propto e^{-\sqrt{p/p_0}}$ . We note that the stretched-exponential scaling is true in the average sense, while individual instances have very different behavior. For easy instances whose corresponding minimum gaps  $\Delta_{\min}$  are large, exponential scaling of the fractional error is found. For

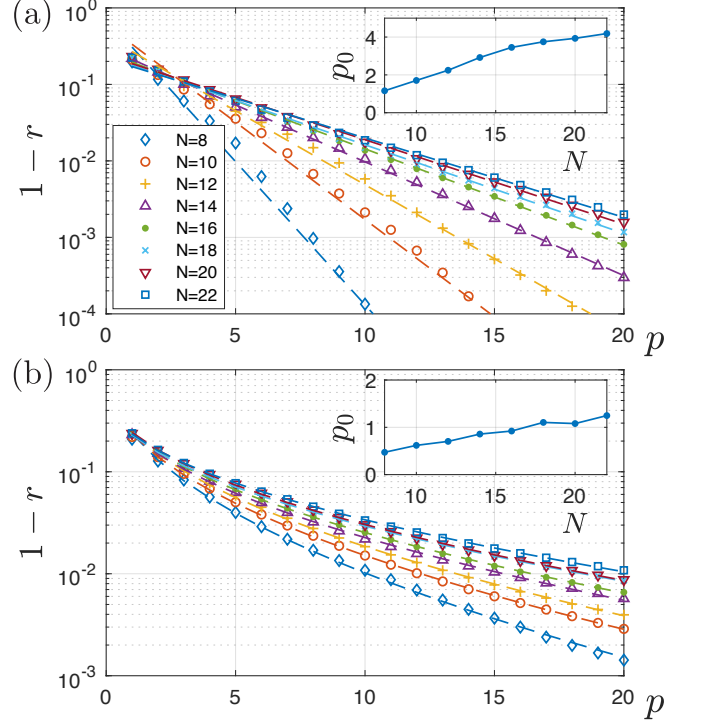


FIG. 4. Average performance of QAOA as measured by the fractional error  $1 - r$ , plotted on log-linear scale. The results are obtained by applying our heuristic optimization strategies FOURIER to up to 100 random instances of (a) u3R graphs and (b) w3R graphs. Differently colored lines correspond to fitted lines to the average for different system size  $N$ , where the model function is  $1 - r \propto e^{-p/p_0}$  for unweighted graphs and  $1 - r \propto e^{-\sqrt{p/p_0}}$  for weighted graphs. Insets show the dependence of the fit parameters  $p_0$  on the system size  $N$ .

more difficult instances whose minimum gaps are small, we find that their fractional errors reach plateaus at intermediate  $p$ , before decreasing further when  $p$  is increased. We analyze these hard instances in more depth in the following Section V. Surprisingly, when we average over randomly generated instances, the fractional error is fitted remarkably well by a stretched-exponential function.

These results of average performance of QAOA are interesting despite considerations of finite-size effect. While the decay constant  $p_0$  does appear to depend on the system size  $N$  as shown in the insets of Fig. 4, our finite-size simulations cannot conclusively determine the exact scaling. Although it remains unknown whether the (stretched)-exponential scaling will start to break down at larger system sizes, if the trend continues to system size of  $N = 100 \sim 1000$ , then QAOA will be practically useful in solving interesting MaxCut instances, better or on par with other known algorithms, in a regime where finding the exact solution will be infeasible. Even if QAOA fails for the worst-case graphs, it can still be practically useful, if it performs well on a randomly chosen graph of large system size.

## V. ADIABATIC MECHANISM, QUANTUM ANNEALING, AND QAOA

In the previous section, we benchmark the performance of QAOA for MaxCut on random graph instances in terms of the approximation ratio  $r$ . Although designed for approximate optimization, QAOA is often able to find the MaxCut configuration—the global optimum of the problem—with a high probability as level  $p$  increases. In this section, we assess the efficiency of the algorithm to find the MaxCut configuration and compare it with quantum annealing. In particular, we find that QAOA is not necessarily limited by the minimum gap in the quantum annealing, and explain a mechanism at work that allows it to overcome the adiabatic limitations.

### A. Comparing QAOA with quantum annealing

A predecessor of QAOA, quantum annealing (QA) has been widely studied for the purpose of solving combinatorial optimization problems [35–38]. To find the MaxCut configuration that maximizes  $\langle H_C \rangle$ , we consider the following simple QA protocol:

$$H_{\text{QA}}(s) = -[sH_C + (1-s)H_B], \quad s = t/T, \quad (10)$$

where  $t \in [0, T]$  and  $T$  is the total annealing time. The initial state is prepared to be the ground state of  $H_{\text{QA}}(s=0)$ , i.e.,  $|\psi(0)\rangle = |+\rangle^{\otimes N}$ . The ground state of the final Hamiltonian,  $H_{\text{QA}}(s=1)$ , corresponds to the solution of the MaxCut problem encoded in  $H_C$  [39]. In adiabatic QA, the algorithm relies on the adiabatic theorem to remain in the instantaneous ground state along the annealing path, and solves the computational problem by finding the ground state at the end. To guarantee success, the necessary run time of the algorithm typically scales as  $T = O(1/\Delta_{\min}^2)$ , where  $\Delta_{\min}$  is the minimum spectral gap [14]. Consequently, adiabatic QA becomes inefficient for instances where  $\Delta_{\min}$  is extremely small. We refer to these graph instances as hard instances (for adiabatic QA).

Beyond the completely adiabatic regime, there is often a tradeoff between the success probability (ground state population  $p_{\text{GS}}(T)$ ) and the run time (annealing time  $T$ ): one can either run the algorithm with a long annealing time to obtain a high success probability or run it multiple times at a shorter time to find the solution at least once. A metric often used to determine the best balance is the time-to-solution (TTS) [14]:

$$\text{TTS}_{\text{QA}}(T) = T \frac{\ln(1-p_d)}{\ln[1-p_{\text{GS}}(T)]} \quad (11)$$

$$\text{TTS}_{\text{QA}}^{\text{opt}} = \min_{T>0} \text{TTS}_{\text{QA}}(T). \quad (12)$$

$\text{TTS}_{\text{QA}}(T)$  measures the time required to find the ground state at least once with the target probability  $p_d$  (taken to

be 99% in this paper), neglecting non-algorithmic overheads such as state-preparation and measurement time. In the adiabatic regime where  $\ln[1-p_{\text{GS}}(T)] \propto T\Delta_{\min}^2$  per Landau-Zener formula [34], we have  $\text{TTS}_{\text{QA}} \propto 1/\Delta_{\min}^2$  which is independent of  $T$ . However, it has been observed in some cases that it can be better to run QA non-adiabatically to obtain a shorter TTS [11–14]. By choosing the best annealing time  $T$ , regardless of adiabaticity, we can determine  $\text{TTS}_{\text{QA}}^{\text{opt}}$  as the minimum algorithmic run time of QA. For QAOA, a similar metric can be defined. The variational parameters  $\gamma_i$  and  $\beta_i$  can be regarded as the time evolved under the Hamiltonians  $H_C$  and  $H_B$ , respectively. One can thus interpret the sum of the variational parameters to be the total “annealing” time, i.e.,  $T_p = \sum_{i=1}^p (|\gamma_i^*| + |\beta_i^*|)$  [40], and define

$$\text{TTS}_{\text{QAOA}}(p) = T_p \frac{\ln(1-p_d)}{\ln[1-p_{\text{GS}}(p)]} \quad (13)$$

$$\text{TTS}_{\text{QAOA}}^{\text{opt}} = \min_{p>0} \text{TTS}_{\text{QAOA}}(p), \quad (14)$$

where  $p_{\text{GS}}(p)$  is the ground state population after the optimal  $p$ -level QAOA protocol. Note this quantity does not take into account of the overhead in finding the optimal parameters. We use  $\text{TTS}_{\text{QAOA}}(p)$  here to benchmark the algorithm, and it should not be taken directly to be the actual experimental run time.

To compare the algorithms, we compute  $\text{TTS}_{\text{QA}}^{\text{opt}}$  and  $\text{TTS}_{\text{QAOA}}^{\text{opt}}$  for many random graph instances. For each even vertex number from  $N = 10$  to  $N = 18$ , we randomly generate 1000 instances of w3R graphs. In Fig. 5(a), we plot the relationship between  $\text{TTS}_{\text{QAOA}}^{\text{opt}}$  and the minimum gap  $\Delta_{\min}$  in quantum annealing for each instance. Most of the random graphs have large gaps ( $\Delta_{\min} \gtrsim 10^{-2}$ ), and we observe that the optimal TTS follows the Landau-Zener prediction of  $1/\Delta_{\min}^2$  for these graphs. This indicates that a quasi-adiabatic parametrization of QAOA is the best when  $\Delta_{\min}$  is reasonably large. Many graphs, however, exhibit very small gaps ( $\Delta_{\min} \lesssim 10^{-3}$ ), and thus require exceedingly long run time for adiabatic evolution. For some graphs,  $\Delta_{\min}$  is as small as  $10^{-8}$ , which implies an adiabatic evolution requires a run time  $T \gtrsim 10^{16}$ . Nevertheless, we see that QAOA can find the solution for these hard instances faster than adiabatic QA. Remarkably,  $\text{TTS}_{\text{QAOA}}^{\text{opt}}$  appears to be independent of the gap for all graphs that have extremely small gaps, and beats the adiabatic TTS (Landau-Zener line) by many orders of magnitude. This suggests that an exponential improvement of TTS is possible with non-adiabatic mechanisms when adiabatic QA is limited by exponentially small gaps.

Similarly for QA, the optimal annealing time  $T$  is often not in the adiabatic limit for small-gap graphs. In Fig. 5(b), we observe a strong correlation between  $\text{TTS}_{\text{QAOA}}^{\text{opt}}$  and  $\text{TTS}_{\text{QA}}^{\text{opt}}$  for each graph instance. This suggests that QAOA is making use of the optimal annealing schedule, regardless of whether a slow adiabatic evolution or a fast diabatic evolution is better. In the

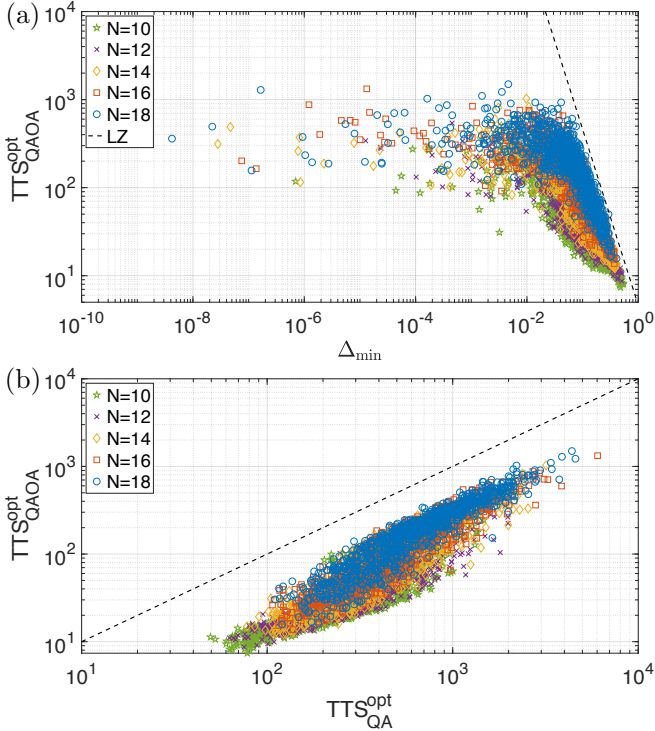


FIG. 5. (a)  $TTS_{QAOA}^{\text{opt}}$  versus the minimum spectral gap in QA,  $\Delta_{\min}$ , for many random w3R graph instances. 1000 random instances are generated for each graph vertex size  $N$ . The maximum cutoff  $p$  is taken to be  $p_{\max} = 50, 50, 40, 35, 30$  for  $N = 10, 12, 14, 16, 18$ , respectively. Dashed line corresponds to adiabatic QA run time of  $1/\Delta_{\min}^2$  predicted by Landau-Zener [34]. (b)  $TTS_{QAOA}^{\text{opt}}$  versus  $TTS_{QA}^{\text{opt}}$  for each random graph instance. QAOA outperforms QA for instances below the dashed line. The (Pearson's) correlation coefficient between QAOA TTS and QA TTS is  $\rho(\ln(TTS_{QAOA}^{\text{opt}}), \ln(TTS_{QA}^{\text{opt}})) \approx 0.91$ .

following subsection, we take a representative example to explain our results observed in Fig. 5 and a mechanism of QAOA to go beyond the adiabatic paradigm.

### B. Beyond the adiabatic mechanism: a case study

To understand the behavior of QAOA, we focus on graph instances that are hard for adiabatic QA in this subsection. In particular, we study a representative instance to explain how QAOA as well as diabatic QA can overcome the adiabatic limitations. As illustrated in Fig. 6(a), we demonstrate that QAOA can learn to utilize diabatic transitions at anti-crossings to circumvent difficulties caused by very small gaps in QA.

Fig. 6(b) shows a representative graph with  $N = 14$ , whose minimum spectral gap  $\Delta_{\min} < 10^{-3}$ . For this example hard instance, we first numerically simulate the quantum annealing process. Fig. 6(c) shows populations in the ground state and low excited states at the end of the process for different annealing time  $T$ . Since the

minimum gap is very small, the adiabatic condition requires  $T \gtrsim 1/\Delta_{\min}^2 \approx 10^6$ . The Landau-Zener formula for the ground state population  $p_{\text{GS}} = 1 - \exp(-cT\Delta_{\min}^2)$  fits well with our exact numerical simulation, where  $c$  is a fitting parameter. However, we can clearly observe a “bump” in the ground state population at annealing time  $T \approx 40$ . At such a time scale, the dynamics is clearly non-adiabatic; we call this phenomenon a *diabatic bump*. This phenomenon has been observed earlier in Ref. [11–14] for other optimization problems.

Subsequently, we simulate QAOA on this hard instance. As mentioned earlier, although QAOA optimizes energy instead of ground state overlap, substantial ground state population can still be obtained even for many hard graphs. Using our FOURIER heuristic strategy, various low-energy state populations of the output state are shown for different levels  $p$  in Fig. 6(d). We observe that QAOA can achieve similar ground state population as the diabatic bump at small  $p$ , and then substantially enhance it after  $p \gtrsim 24$ .

To better understand the mechanism of QAOA and make a meaningful comparison with QA, we can interpret the QAOA parameters as a smooth annealing path. We again interpret the sum of the variational parameters to be the total annealing time, i.e.,  $T_p = \sum_{i=1}^p (|\gamma_i| + |\beta_i|)$ . A smooth annealing path can be constructed from QAOA optimal parameters as

$$H_{\text{QAOA}}(t) = -[f(t)H_C + (1 - f(t))H_B], \quad (15)$$

$$f\left(t_i = \sum_{j=1}^i (|\gamma_j^*| + |\beta_j^*|) - \frac{1}{2}(|\gamma_i^*| + |\beta_i^*|)\right) = \frac{\gamma_i^*}{|\gamma_i^*| + |\beta_i^*|},$$

where  $t_i$  is chosen to be at the mid-point of each time interval  $(\gamma_i^* + \beta_i^*)$ . With the boundary conditions  $f(t=0) = 0$ ,  $f(t=T_p) = 1$  and linear interpolation at other intermediate time  $t$ , we can convert QAOA parameters to a well-defined annealing path. We apply this conversion to the QAOA optimal parameters at  $p = 40$  [Fig. 6(e)]. With this annealing path, we can follow the instantaneous eigenstate population throughout the quantum annealing process [Fig. 6(f)]. In contrast to adiabatic QA, the state population leaks out of the ground state and accumulates in the first excited state before the anti-crossing point, where the gap is at its minimum. Using a diabatic transition at the anti-crossing, the two states swap populations, and a large ground state population is obtained in the end. We note that the final state population from the constructed annealing path differs slightly from those of QAOA, due to Trotterization and interpolation, but the underlying mechanism is the same, which is also responsible for the diabatic bump seen in Fig. 6(c). In addition to the conversion used in Eq. (15), we have tested a few other prescriptions to construct an annealing path from QAOA parameters, and qualitative features do not seem to change.

Hence, our results indicate that QAOA is closely related to a cleverly optimized diabatic QA path that

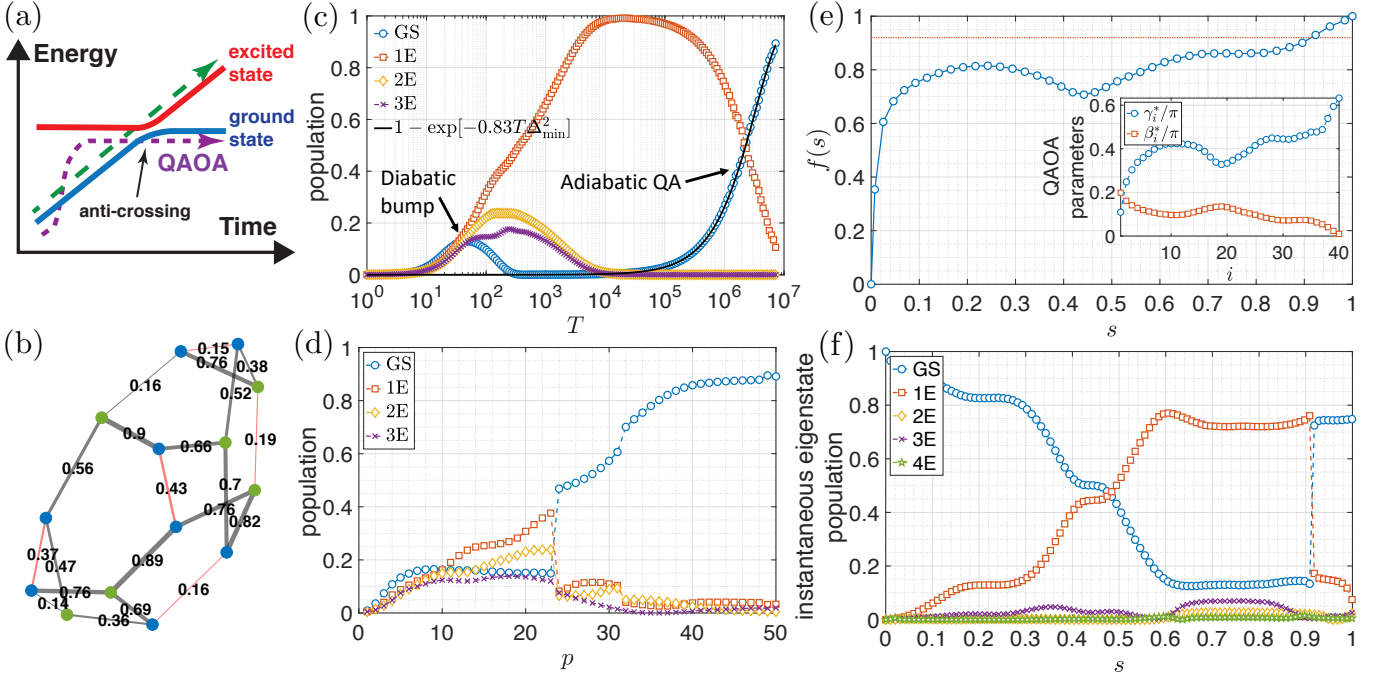


FIG. 6. (a) A schematic of how QAOA and the interpolated annealing path can overcome the small minimum gap limitations via diabatic transitions (purple line). Naive adiabatic quantum annealing path leads to excited states passing through the anti-crossing point (green line). (b) An instance of weighted 3-regular graph that has a small minimum spectral gap along the quantum annealing path given by Eq. (10). The optimal MaxCut configuration is shown with two vertex colors, and the black (red) lines are the cut (uncut) edges. (c) Population in low excited states after the quantum annealing protocol with different total time  $T$ . The black solid line follows the Landau-Zener formula for the ground state population,  $p_{GS} = 1 - \exp(-cT\Delta_{\min}^2)$ , where  $c$  is a fitting parameter. (d) Population in low excited states using QAOA at different level  $p$ . The FOURIER heuristic strategy is used in the optimization. (e) Interpreting QAOA parameters (at  $p = 40$ ) as a smooth quantum annealing path, via linear interpolation according to Eq. (15). The annealing time parameter  $s = t/T_p$ , where  $T_p = \sum_{i=1}^p (|\gamma_i^*| + |\beta_i^*|)$ . The red dotted line labels the location of anti-crossing where the gap is at its minimum, at which point  $f(s) \approx 0.92$ . Inset shows the original QAOA optimal parameters  $\gamma_i^*/\pi$  and  $\beta_i^*/\pi$  for  $p = 40$ . (f) Instantaneous eigenstate population under the annealing path given in (e). Note that the instantaneous ground state and first excited state swap at the anti-crossing point.

can overcome limitations set by the adiabatic theorem. Through optimization, QAOA can find a good annealing path and exploit diabatic transitions to enhance ground state population. This explains the observation in Fig. 5(a) that  $TTS_{\text{QAOA}}^{\text{opt}}$  can be significantly shorter than the time required by the adiabatic algorithm. On the other hand, as seen in Fig. 5(b),  $TTS_{\text{QAOA}}^{\text{opt}}$  is strongly correlated with  $TTS_{\text{QA}}^{\text{opt}}$ : QAOA automatically finds a good annealing path, which could be adiabatic or not, depending on what is the best route for the specific problem instance.

The effective dynamics of QAOA for this specific instance, as we see in Fig. 6(f), can be understood mostly by an effective two-level system (see Appendix D for more discussions). In general, the energy spectrum can be more complex, and the dynamics may involve many excited states, which may not be explainable by the simple schematic in Fig. 6(a). Nonetheless, QAOA can find a suitable path via our heuristic optimization strategies even in more complicated cases [41].

## VI. CONSIDERATIONS FOR EXPERIMENTAL IMPLEMENTATION

In this section, we discuss some important considerations for experimental realization. The framework of QAOA is general and can be applied to various experimental platforms to solve combinatorial optimization problems. Here, we again focus on the MaxCut problem as a paradigmatic example, although it can also be applied to solve other interesting problems [41, 42].

### A. Finite measurement samples

So far, we have focused on understanding the best theoretically possible performance of QAOA, and assumed perfect measurement precision of the objective function in our numerical simulations. However, due to quantum fluctuations (i.e., projection noise) in actual experiments, the precision is finite since it is obtained via averaging over finitely many measurement outcomes that can only take on discrete values. Hence, in practice, there is

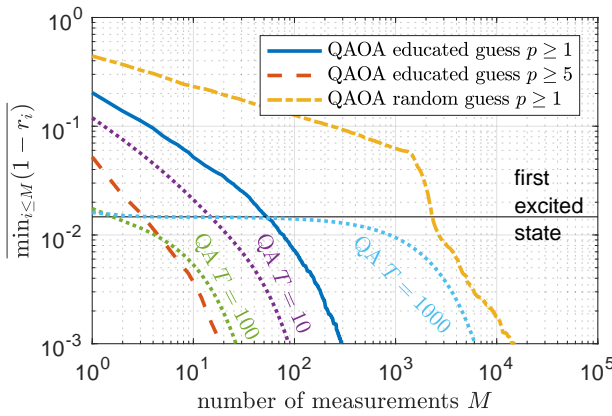


FIG. 7. Full Monte-Carlo simulation of QAOA accounting for measurement projection noise, on the example instance studied in Fig. 6(b). For various optimization strategies, we keep track of approximation ratio  $r_i = |\text{Cut}_i|/|\text{MaxCut}|$  from the  $i$ -th measurement, and plot minimum fractional error  $1 - r_i$  found after  $M$  measurements, averaged over many Monte-Carlo realizations. The blue solid and red dashed lines correspond to QAOA optimized with the FOURIER strategy starting with an educated guess of  $(\vec{\gamma}, \vec{\beta})$  at  $p = 1$  and  $p = 5$ , respectively. The orange dash-dot line corresponds to QAOA optimized starting with random guesses at  $p = 1$ . The three labelled dotted lines are results from QA with total time  $T = 10^2, 10^3$ .

a trade-off between measurement cost and optimization quality: finding good optimum requires good precision at the cost of large number of measurements [43]. Additionally, large variance in the objective function value demands more measurements, but may help improve the chances of finding near-optimal MaxCut configurations.

Here, we study the effect of measurement projection noise with a full Monte-Carlo simulation of QAOA on some example graphs, where objective function is evaluated by repeated projective measurements until its error is below a threshold. More implementation details of this numerical simulation are discussed in Appendix E. In Fig. 7, we present the Monte-Carlo simulation result for the example instance studied earlier in Fig. 6(b). Here, we simulate QAOA optimized with our FOURIER heuristic starting at level either  $p=1$  or  $p=5$  using an educated choice of initial parameters based on known optima found for small size instances. We see that QAOA can find the MaxCut solution in  $\sim 10\text{--}10^2$  measurements, and starting our optimization at intermediate level ( $p=5$ ) is better than starting at the lowest level ( $p=1$ ). In comparison, random choices of initial parameters starting at  $p=1$  perform much worse, which fails to find the MaxCut solution until  $10^3\text{--}10^4$  measurements have been made. Moreover, when we compare QAOA to QA with various annealing time, it appears that the choice of annealing time  $T=100$  can perform just as well as QAOA on this instance. Nevertheless, running QAOA at level  $p=5$  is still more advantageous than QA

at  $T=100$ , when coherence time is limited.

We remark that our simulation is only limited to small-size instances, and the good performance of QAOA and QA we observe is complicated by the small but significant ground state population from generic annealing schedules. Since it often takes  $10^2$  measurements to obtain a sufficiently precise estimate of the objective function, a ground state probability of  $\gtrsim 10^{-2}$  would mean that one can find the ground state without much parameter optimization. Nevertheless, as quantum computers with  $10^2 \sim 10^3$  qubits begin to come online, it will be interesting to see how QAOA performs on much larger instances where the ground state probability from generic QAOA/QA protocol is expected to be exponentially small, whereas the number of measurements necessary for optimization grows only polynomially with problem size. The results here indicate that the parameter pattern and our heuristic strategies are practically useful guidelines in realistic implementation of QAOA.

## B. Implementation for large problem sizes

As experiments begin to test solving the MaxCut problems with quantum machines [6], limited quantum coherence time and graph connectivity will be among the biggest challenges. In terms of coherence time, QAOA is highly advantageous: the hybrid nature of QAOA as well as its short- and intermediate-depth circuit parametrization makes it ideal for near-term quantum devices. In addition, we have demonstrated that QAOA is not generally limited by the small spectral gaps, which raises hopes to (approximately) solve interesting problems within the coherence time.

What would be the necessary problem size to explore a meaningful quantum advantage? We note that one of the leading exact classical solver, the BiqMac solver [44], is able to solve MaxCut exactly up to  $N \lesssim 100$ , but takes a long time (more than an hour) for larger problem sizes. A fast heuristic algorithm, the breakout local search algorithm [45], can find the MaxCut solution with a high probability for problem size of a few hundreds, although the solution is not guaranteed. Hence, a MaxCut problem with a few hundred vertices will be an interesting regime to benchmark quantum algorithms. In terms of approximation, we have noted earlier that the polynomial-time Goemans-Williamson algorithm has an approximation ratio guarantee of  $r^* \approx 0.878$ . It will be also interesting to find out if QAOA is able to achieve a better approximation ratio for some problem instances where the exact solution is not obtainable, in this regime of hundreds of vertices.

We now discuss a few considerations that put these large-size problems in the experimentally feasible regime on near-term quantum systems.

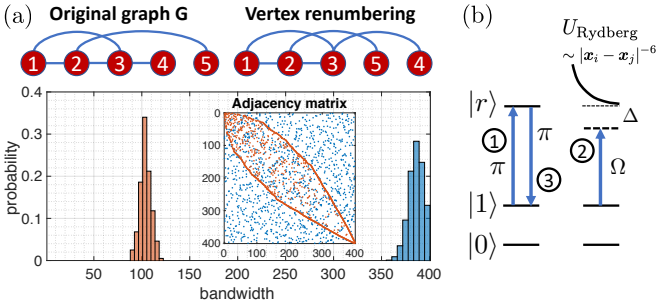


FIG. 8. (a) Vertex renumbering to reduce the graph bandwidth. Top panel: an example of vertex renumbering for a 5-vertex graph. Bottom panel: distribution of graph bandwidths for 1000 random 3-regular graphs with  $N = 400$  each. The blue (orange) bars are the bandwidth before (after) vertex renumbering. Inset shows the sparsity pattern of the adjacency matrix before and after vertex renumbering for one particular graph. (b) A protocol to use Rydberg-blockade controlled gate to implement the interaction term  $\exp(-i\gamma\sigma_i^z\sigma_j^z)$ . By choosing a proper gate time for the second step ( $t = 2\pi/\sqrt{\Omega^2 + \Delta^2}$ ), one does not accumulate population on the Rydberg level  $|r\rangle$ . With tunable coupling strength  $\Omega$  and detuning  $\Delta$ , one can control the interaction time  $\gamma$ .

### 1. Reducing interaction range

In a quantum experiment, each vertex can be represented by a qubit. For a large problem size, a major challenge to encode general graphs will be the necessary range and versatility of the interaction patterns (between qubits). The embedding of a random graph into a physical implementation with a 1D or 2D geometry may require very long-range interactions. By relabelling the graph vertices, one can actually reduce the required range of interactions. This can be formulated as the *graph bandwidth problem*: Given a graph  $G = (V, E)$  with  $N$  vertices, a vertex numbering is a bijective map from vertices to distinct integers,  $f : V \rightarrow \{1, 2, \dots, N\}$ . The bandwidth of a vertex numbering  $f$  is  $B_f(G) = \max\{|f(u) - f(v)| : (u, v) \in E(G)\}$ , which can be understood as the length of the longest edge (in 1D). The graph bandwidth problem is then to find the minimum bandwidth among all vertex numberings, i.e.,  $B(G) = \min_f B_f(G)$ ; namely, it is to minimize the length of the longest edge by vertex renumbering.

In general, finding the minimum graph bandwidth is NP-hard, but good heuristic algorithms have been developed to reduce the graph bandwidth. Fig. 8(a) shows a simple example of bandwidth reduction. The top panel illustrates the vertex renumbering with a 5-vertex graph. The bottom panel shows the histogram of graph bandwidths for 1000 random 3-regular graphs of  $N = 400$  each. Using the Cuthill-McKee algorithm [46], the graph bandwidth can be reduced to around  $B \approx 100$ . While this still requires quite a long interaction range in 1D, the bandwidth problem can also be generalized to higher dimensions. In 2D arrangements, we then expect the

radius of interaction to be  $B_{2D} \sim \sqrt{100}$  for  $N = 400$  3-regular graphs [47], which seems within reach for near-term quantum devices. A detailed study of the 2D bandwidth problem is beyond the scope of this work. Alternatively, one can make use of a general construction to encode any long-range interactions to local fields [48], although it requires additional physical qubits and gauge constraints. Apart from implementing arbitrary graphs in full generality, one can also restrict to special graphs that exhibit some geometric structures. For example, unit disk graphs are geometric graphs in the 2D plane, where vertices are connected by an edge only if they are within a unit distance. These graphs can be more naturally encoded into 2D physical implementations, and the MaxCut problem is still NP-hard on unit disk graphs [49].

### 2. Example Implementation with Rydberg Atoms

The above discussion has been experimental-platform independent, and is applicable to any state-of-the-art platforms, such as neutral Rydberg atoms [15, 16, 50–52], trapped ions [7, 53–55], and superconducting qubits [6, 56, 57]. As an example, we briefly describe a feasible implementation of QAOA with neutral atoms interacting via Rydberg excitations, where high-fidelity entanglement has been recently demonstrated [58]. We can use the hyperfine ground states in each atom to encode the qubit states  $|0\rangle$  and  $|1\rangle$ , and the  $|1\rangle$  state can be excited to the Rydberg level  $|r\rangle$  to induce interactions. The qubit rotating term,  $\exp(-i\beta\sum_{j=1}^N\sigma_j^x)$ , can be implemented straightforwardly by a global driving beam with tunable durations. The interaction terms  $\sum_{\langle i,j \rangle}\sigma_i^z\sigma_j^z$  can be implemented stroboscopically for general graphs; this can be realized by a Rydberg-blockade controlled gate [16], as illustrated in Fig. 8(b). By controlling the coupling strength  $\Omega$ , detuning  $\Delta$ , and the gate time, together with single-qubit rotations, one can implement  $\exp(-i\gamma\sigma_i^z\sigma_j^z)$ , which can then be repeated for each interacting pair. An additional major advantage of the Rydberg-blockade mechanism is its ability to perform multi-qubit collective gates in parallel [16, 59]. This can reduce the number of two-qubit operation steps from the number of edges to the number of vertices,  $N$ , which means a factor of  $N$  reduction for dense graphs with  $\sim N^2$  edges. While the falloff of Rydberg interactions may limit the distance two qubits can interact, MaxCut problems of interesting sizes can still be implemented by vertex renumbering or focusing on unit disk graphs, as discussed above.

For generic problems of 400-vertex regular graphs, we expect the necessary interaction range to be 5 atoms in 2D; assuming minimum inter-atom separation of  $2 \mu\text{m}$ , this means an interaction radius of  $10 \mu\text{m}$ , which is realizable with high Rydberg levels [16]. Given realistic estimates of coupling strength  $\Omega \sim 2\pi \times 10\text{-}100 \text{ MHz}$  and single-qubit coherence time  $\tau \sim 200 \mu\text{s}$  (limited by Rydberg level lifetime), we expect with high-fidelity con-

trol, the error per two-qubit gate can be made roughly  $(\Omega\tau)^{-1} \sim 10^{-3}\text{--}10^{-4}$ . For 400-vertex 3-regular graphs, we can implement QAOA of level  $p \simeq \Omega\tau/N \sim 25$  with a 2D array of neutral atoms. We note that these are conservative estimates since we do not consider advanced control techniques such as pulse-shaping, and require less than one error in the entire quantum circuit; it is possible that QAOA is not sensitive to some of the imperfections. Hence, we envision that soon, QAOA can be benchmarked against classical [21, 44, 45] and semiclassical [60–62] solvers on large problem sizes with near-term quantum devices.

## VII. CONCLUSION AND OUTLOOK

In summary, we have studied the performance, non-adiabatic mechanism, and practical implementation of QAOA applied to the MaxCut problems. Based on the observed patterns in the QAOA optimal parameters, we developed heuristic strategies to efficiently find quasi-optimal parameters in  $O(\text{poly}(p))$  time, whereas  $2^{O(p)}$  number of brute-force runs is needed to obtain an equally good solution. We benchmarked, using these heuristic optimization strategies, the performance of QAOA up to  $p \leq 50$ . On average, the performance characterized by the approximation ratio was observed to improve exponentially (or stretched-exponentially) for random unweighted (or weighted) graphs. Focusing on hard graph instances where adiabatic QA fails due to extremely small spectral gaps, we found that QAOA could learn via optimization a diabatic path to achieve significantly higher success probabilities to find the MaxCut solution. A metric taking into account of both the success probability and the run time indicates QAOA may not be limited by small spectral gaps. Finally, we provided a detailed resource analysis for experimental implementation of QAOA on MaxCut and proposed a neutral-atom realization where a problem size of a few hundred atoms are feasible in the near future.

As we have benchmarked via random MaxCut instances, our simple heuristic optimization strategies work very well. Nevertheless, more sophisticated methods could be developed to improve the performance and robustness. One possibility would be using machine learning techniques to automatically learn and make use of the optimal parameter patterns to develop even more efficient parametrization and strategies (see e.g., [63]). Another important but unsettled problem is assessing a reliable system-size scaling for QAOA. On average, we observed (stretched) exponential improvement with level  $p$ , up to  $N = 22$ . It remains open whether the same scaling will persist for larger system size. For the hard instances we generated that have exceedingly small spectral gaps, QAOA is able to overcome the adiabatic limitations in all

cases examined; it remains to be seen how this behavior could extrapolate to larger problems. An experimental implementation with near-term quantum devices will be able to push the limit of our understanding and serve as a litmus test for genuine quantum speedup in solving practical problems.

Besides MaxCut, another interesting optimization problem is the Maximum Independent Set (MIS) problem, which is also NP-hard and has many real-world applications [64, 65]. In a separate work [41], we show that the MIS problem can be naturally encoded into the ground state of neutral atoms interacting via Rydberg excitations, with almost no overhead on the hardware. The methodology we have developed here for QAOA on MaxCut can be directly adapted to the MIS problem. With such rapid development in near-term quantum computer, we will soon be able to witness experimental tests of the capability of quantum algorithms to solve practically interesting problems.

## ACKNOWLEDGMENTS

We thank Edward Farhi, Aram Harrow, Peter Zoller, Ignacio Cirac, Jeffrey Goldstone, Sam Gutmann, Wen Wei Ho, and Dries Sels for fruitful discussions. S.-T.W. in addition would like to thank Daniel Lidar, Matthias Troyer, and Johannes Otterbach for insightful discussions and suggestions during the Aspen Winter Conference on Advances in Quantum Algorithms and Computation. This work was supported through the National Science Foundation (NSF), the Center for Ultracold Atoms, the Air Force Office of Scientific Research via the MURI, the Vannevar Bush Faculty Fellowship, DOE, and Google Research Award. S.C. acknowledges support from the Miller Institute for Basic Research in Science. H.P. is supported by the NSF through a grant for the Institute for Theoretical Atomic, Molecular, and Optical Physics at Harvard University and the Smithsonian Astrophysical Observatory. Some of the computations in this paper were performed on the Odyssey cluster supported by the FAS Division of Science, Research Computing Group at Harvard University.

*Note added.*—After the completion of this work, we became aware of a related work appearing in Ref. [66]. In the preprint, they trained the QAOA variational parameters on a batch of graph instances and compared QAOA’s performance with the classical Goemans-Williamson algorithm on small-size MaxCut problems. Similar parameter shapes were found, but Ref. [66] did not make use of any observed patterns to design optimization strategies. We, in addition, discovered non-adiabatic mechanisms of QAOA, which is not studied in Ref. [66].

---

[1] J. Preskill, *Quantum* **2**, 79 (2018).

[2] E. Farhi, J. Goldstone, and S. Gutmann, (2014), [arXiv:1411.4028](https://arxiv.org/abs/1411.4028).

[3] A. Peruzzo, J. McClean, P. Shadbolt, M.-H. Yung, X.-Q. Zhou, P. J. Love, A. Aspuru-Guzik, and J. L. O’Brien, *Nature Communications* **5**, 4213 (2014).

[4] N. Moll, P. Barkoutsos, L. S. Bishop, J. M. Chow, A. Cross, D. J. Egger, S. Filipp, A. Fuhrer, J. M. Gambetta, M. Ganzhorn, A. Kandala, A. Mezzacapo, P. Müller, W. Riess, G. Salis, J. Smolin, I. Tavernelli, and K. Temme, *Quantum Science and Technology* **3**, 030503 (2018).

[5] A. Kandala, A. Mezzacapo, K. Temme, M. Takita, M. Brink, J. M. Chow, and J. M. Gambetta, *Nature* **549**, 242 (2017).

[6] J. S. Otterbach, R. Manenti, N. Alidoust, A. Bestwick, M. Block, B. Bloom, S. Caldwell, N. Didier, E. Schuyler Fried, S. Hong, P. Karalekas, C. B. Osborn, A. Parageorge, E. C. Peterson, G. Prawiroatmodjo, N. Rubin, C. A. Ryan, D. Scarabelli, M. Scheer, E. A. Sete, P. Sivarajah, R. S. Smith, A. Staley, N. Tezak, W. J. Zeng, A. Hudson, B. R. Johnson, M. Reagor, M. P. da Silva, and C. Rigetti, (2017), [arXiv:1712.05771](https://arxiv.org/abs/1712.05771).

[7] C. Kokail, C. Maier, R. van Bijnen, T. Brydges, M. K. Joshi, P. Jurcevic, C. A. Muschik, P. Silvi, R. Blatt, C. F. Roos, and P. Zoller, (2018), [arXiv:1810.03421](https://arxiv.org/abs/1810.03421).

[8] E. Farhi, J. Goldstone, and S. Gutmann, (2014), [arXiv:1412.6062](https://arxiv.org/abs/1412.6062).

[9] E. Farhi and A. W. Harrow, (2016), [arXiv:1602.07674](https://arxiv.org/abs/1602.07674).

[10] J. R. McClean, S. Boixo, V. N. Smelyanskiy, R. Babbush, and H. Neven, *Nature Communications* **9**, 4812 (2018).

[11] E. Crosson, E. Farhi, C. Y.-Y. Lin, H.-H. Lin, and P. Shor, (2014), [arXiv:1401.7320](https://arxiv.org/abs/1401.7320).

[12] S. Muthukrishnan, T. Albash, and D. A. Lidar, *Phys. Rev. X* **6**, 031010 (2016).

[13] L. Hormozi, E. W. Brown, G. Carleo, and M. Troyer, *Phys. Rev. B* **95**, 184416 (2017).

[14] T. Albash and D. A. Lidar, *Rev. Mod. Phys.* **90**, 015002 (2018).

[15] H. Bernien, S. Schwartz, A. Keesling, H. Levine, A. Omran, H. Pichler, S. Choi, A. S. Zibrov, M. Endres, M. Greiner, V. Vuletić, and M. D. Lukin, *Nature* **551**, 579 (2017).

[16] M. Saffman, T. G. Walker, and K. Mølmer, *Rev. Mod. Phys.* **82**, 2313 (2010).

[17] C. H. Papadimitriou and K. Steiglitz, *Combinatorial optimization: algorithms and complexity* (Courier Corporation, 1998).

[18] B. Korte, J. Vygen, B. Korte, and J. Vygen, *Combinatorial optimization*, Vol. 2 (Springer, 2012).

[19] J. Håstad, *J. ACM* **48**, 798 (2001).

[20] P. Berman and M. Karpinski (Springer, Berlin, Heidelberg, 1999) pp. 200–209.

[21] M. X. Goemans and D. P. Williamson, *J. ACM* **42**, 1115 (1995).

[22] E. Halperin, D. Livnat, and U. Zwick, *Journal of Algorithms* **53**, 169 (2004).

[23] Z. Wang, S. Hadfield, Z. Jiang, and E. G. Rieffel, *Phys. Rev. A* **97**, 022304 (2018).

[24] D. Wecker, M. B. Hastings, and M. Troyer, *Phys. Rev. A* **94**, 022309 (2016).

[25] Z.-C. Yang, A. Rahmani, A. Shabani, H. Neven, and C. Chamon, *Phys. Rev. X* **7**, 021027 (2017).

[26] W. W. Ho and T. H. Hsieh, (2018), [arXiv:1803.00026](https://arxiv.org/abs/1803.00026) [cond-mat.str-el].

[27] Z. Jiang, E. G. Rieffel, and Z. Wang, *Phys. Rev. A* **95**, 062317 (2017).

[28] E. R. Anschuetz, J. P. Olson, A. Aspuru-Guzik, and Y. Cao, ArXiv e-prints (2018), [arXiv:1808.08927](https://arxiv.org/abs/1808.08927).

[29] The approximation ratio  $r = (2p+1)/(2p+2)$  is found for an infinite ring. For a finite ring with  $N$  vertices, numerical calculations show that for  $p < \lfloor N/2 \rfloor$  one has  $r = (2p+1)/(2p+2)$  for even  $N$  and  $r = \frac{(2p+1)(N+1)}{(2p+2)^N}$  for odd  $N$ , and for  $p \geq \lfloor N/2 \rfloor$  one has  $r = 1$ .

[30] C. G. Broyden, *IMA Journal of Applied Mathematics* **6**, 76 (1970); R. Fletcher, *The Computer Journal* **13**, 317 (1970); D. Goldfarb, *Mathematics of Computation* **24**, 23 (1970); D. F. Shanno, *Mathematics of Computation* **24**, 647 (1970).

[31] The starting points  $\beta_i^0$  are drawn uniformly from  $[-\frac{\pi}{4}, \frac{\pi}{4}]$ , and  $\gamma_i^0$  are drawn uniformly  $[-\frac{\pi}{2}, \frac{\pi}{2}]$  for u3R graphs or  $[-2\pi, 2\pi]$  for w3R graphs. Although  $\gamma_i^0$  can meaningfully take values beyond the restricted range  $\gamma_i^0 \in [-2\pi, 2\pi]$  for w3R graph, we find that broadening the range does not improve performance. Note the ranges of the output parameters are not restricted in our unconstrained optimization algorithm.

[32] We denote the best of all local optima optimized from  $k$  random starting points (seeds) to be  $(\vec{\gamma}^{B[k]}, \vec{\beta}^{B[k]})$ . When the same optimum  $(\vec{\gamma}^{B[k]}, \vec{\beta}^{B[k]})$  is found from many different seeds and continues to yield the best  $F_p(\vec{\gamma}^{B[k]}, \vec{\beta}^{B[k]})$  as we increase the number of seeds  $k$ , we then claim that it is a global optimum, i.e.,  $(\vec{\gamma}^*, \vec{\beta}^*) = \lim_{k \rightarrow \infty} (\vec{\gamma}^{B[k]}, \vec{\beta}^{B[k]})$ .

[33] J. A. Nelder and R. Mead, *The Computer Journal* **7**, 308 (1965).

[34] Landau and L. D., *Z. Sowjetunion* **2**, 46 (1932); C. Zener, *Proc. R. Soc. London, Ser. A* **137**, 696 (1932).

[35] T. Kadokawa and H. Nishimori, *Phys. Rev. E* **58**, 5355 (1998).

[36] E. Farhi, J. Goldstone, S. Gutmann, J. Lapan, A. Lundgren, and D. Preda, *Science* **292**, 472 (2001).

[37] S. Boixo, T. F. Rønnow, S. V. Isakov, Z. Wang, D. Wecker, D. A. Lidar, J. M. Martinis, and M. Troyer, *Nature Physics* **10**, 218 (2014).

[38] T. F. Rønnow, Z. Wang, J. Job, S. Boixo, S. V. Isakov, D. Wecker, J. M. Martinis, D. A. Lidar, and M. Troyer, *Science* **345**, 420 (2014).

[39] To be consistent with the language of QA, here we use the terminology of ground state and low excited states of  $-H_C$  instead of referring to them as highest excited states in the MaxCut language.

[40] This could change with different normalizations of the Hamiltonians  $H_C$  and  $H_B$ , but our qualitative results remain the same. The physical limitation in the experiment is typically the interaction strength in  $H_C$ .

[41] H. Pichler, S.-T. Wang, L. Zhou, S. Choi, and M. D. Lukin, (2018), [arXiv:1808.10816](https://arxiv.org/abs/1808.10816).

[42] H. Pichler, S.-T. Wang, L. Zhou, S. Choi, and M. D. Lukin, (2018), [arXiv:1809.04954](https://arxiv.org/abs/1809.04954).

[43] G. Giacomo Guerreschi and M. Smelyanskiy, (2017), [arXiv:1701.01450](https://arxiv.org/abs/1701.01450).

[44] F. Rendl, G. Rinaldi, and A. Wiegele, *Mathematical Programming* **121**, 307 (2008).

[45] U. Benlic and J.-K. Hao, *Engineering Applications of Artificial Intelligence* **26**, 1162 (2013).

[46] E. Cuthill and J. McKee, in *Proceedings of the 1969 24th National Conference*, ACM '69 (ACM, New York, NY, USA, 1969) pp. 157–172.

[47] L. Lin and Y. Lin, *RAIRO - Theoretical Informatics and Applications* **45**, 399 (2011).

[48] W. Lechner, P. Hauke, and P. Zoller, *Science Advances* **1** (2015).

[49] J. Díaz and M. Kamiński, *Theoretical Computer Science* **377**, 271 (2007).

[50] H. Labuhn, D. Barredo, S. Ravets, S. de Léséleuc, T. Macrì, T. Lahaye, and A. Browaeys, *Nature* **534**, 667 (2016).

[51] A. Keesling, A. Omran, H. Levine, H. Bernien, H. Pichler, S. Choi, R. Samajdar, S. Schwartz, P. Silvi, S. Sachdev, P. Zoller, M. Endres, M. Greiner, V. Vuletić, and M. D. Lukin, (2018), [arXiv:1809.05540](https://arxiv.org/abs/1809.05540).

[52] A. Kumar, T.-Y. Wu, F. Giraldo, and D. S. Weiss, *Nature* **561**, 83 (2018).

[53] H. Häffner, C. Roos, and R. Blatt, *Physics Reports* **469**, 155 (2008).

[54] S. Debnath, N. M. Linke, C. Figgatt, K. A. Landsman, K. Wright, and C. Monroe, *Nature* **536**, 63 (2016).

[55] J. Zhang, G. Pagano, P. W. Hess, A. Kyprianidis, P. Becker, H. Kaplan, A. V. Gorshkov, Z. X. Gong, and C. Monroe, *Nature* **551**, 601 (2017).

[56] R. Barends, A. Shabani, L. Lamata, J. Kelly, A. Mezzacapo, U. L. Heras, R. Babbush, A. G. Fowler, B. Campbell, Y. Chen, Z. Chen, B. Chiaro, A. Dunsworth, E. Jeffrey, E. Lucero, A. Megrant, J. Y. Mutus, M. Neeley, C. Neill, P. J. J. O’Malley, C. Quintana, P. Roushan, D. Sank, A. Vainsencher, J. Wenner, T. C. White, E. Solano, H. Neven, and J. M. Martinis, *Nature* **534**, 222 (2016).

[57] C. Neill, P. Roushan, K. Kechedzhi, S. Boixo, S. V. Isakov, V. Smelyanskiy, A. Megrant, B. Chiaro, A. Dunsworth, K. Arya, R. Barends, B. Burkett, Y. Chen, Z. Chen, A. Fowler, B. Foxen, M. Giustina, R. Graff, E. Jeffrey, T. Huang, J. Kelly, P. Klimov, E. Lucero, J. Mutus, M. Neeley, C. Quintana, D. Sank, A. Vainsencher, J. Wenner, T. C. White, H. Neven, and J. M. Martinis, *Science* **360**, 195 (2018).

[58] H. Levine, A. Keesling, A. Omran, H. Bernien, S. Schwartz, A. S. Zibrov, M. Endres, M. Greiner, V. Vuletić, and M. D. Lukin, *Phys. Rev. Lett.* **121**, 123603 (2018).

[59] L. Isenhower, M. Saffman, and K. Mølmer, *Quantum Information Processing* **10**, 755 (2011).

[60] T. Inagaki, Y. Haribara, K. Igarashi, T. Sonobe, S. Tamate, T. Honjo, A. Marandi, P. L. McMahon, T. Umeki, K. Enbusu, O. Tadanaga, H. Takenouchi, K. Aihara, K.-i. Kawarabayashi, K. Inoue, S. Utsunomiya, and H. Takesue, *Science* (2016).

[61] P. L. McMahon, A. Marandi, Y. Haribara, R. Hamerly, C. Langrock, S. Tamate, T. Inagaki, H. Takesue, S. Utsunomiya, K. Aihara, R. L. Byer, M. M. Fejer, H. Mabuchi, and Y. Yamamoto, *Science* (2016).

[62] R. Hamerly, T. Inagaki, P. L. McMahon, D. Venturelli, A. Marandi, T. Onodera, E. Ng, C. Langrock, K. Inaba, T. Honjo, K. Enbusu, T. Umeki, R. Kasahara, S. Utsunomiya, S. Kako, K.-i. Kawarabayashi, R. L. Byer, M. M. Fejer, H. Mabuchi, D. Englund, E. Rieffel, H. Takesue, and Y. Yamamoto, (2018), [arXiv:1805.05217](https://arxiv.org/abs/1805.05217).

[63] M. Bukov, A. G. R. Day, D. Sels, P. Weinberg, A. Polkovnikov, and P. Mehta, *Phys. Rev. X* **8**, 031086 (2018).

[64] A. Vahdatpour, F. Dabiri, M. Moazeni, and M. Sarrafzadeh, in *Distributed Computing* (Springer, Berlin, Heidelberg, Berlin, Heidelberg, 2008) pp. 481–495.

[65] P. K. Agarwal, M. van Kreveld, and S. Suri, *Computational Geometry* **11**, 209 (1998).

[66] G. E. Crooks, (2018), [arXiv:1811.08419](https://arxiv.org/abs/1811.08419).

[67] C. Moler and C. Van Loan, *SIAM Review* **45**, 3 (2003).

[68] R. B. Sidje, *ACM Trans. Math. Softw.* **24**, 130 (1998).

[69] A. H. Al-Mohy and N. J. Higham, *SIAM Journal on Scientific Computing* **33**, 488 (2011).

[70] N. Khaneja, T. Reiss, C. Kehlet, T. Schulte-Herbrüggen, and S. J. Glaser, *Journal of Magnetic Resonance* **172**, 296 (2005).

## Appendix A: Brute-force search and parameter pattern for weighed graphs

Here, we illustrate the pattern of optimal QAOA parameters for weighted 3-regular graphs, analogous to the results of unweighted graphs in Fig. 2(b). This is shown by simultaneously plotting the optimal parameters for 40 instances in Fig. 9. We observe that the spread of  $\vec{\gamma}^*$  for weighted graphs is wider than that for unweighted graphs [see Fig. 2(b)]. This is because the random weights effectively increase the number of subgraph types. Moreover, the larger value for  $\vec{\gamma}^*$  for weighted graph compared to unweighted graphs can be understood via the effective mean-field strength that each qubit experiences.

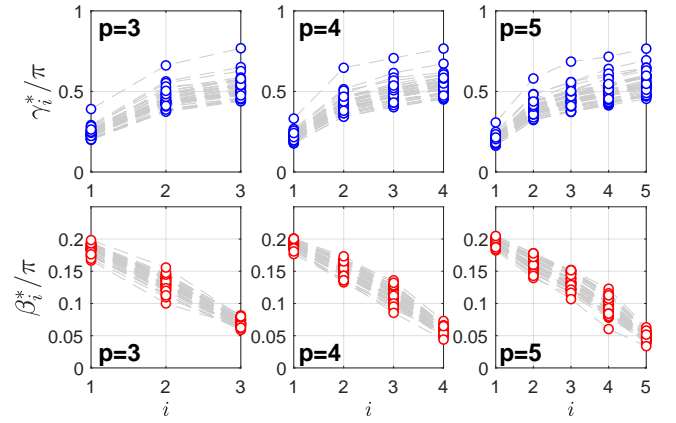


FIG. 9. Optimal QAOA parameters  $(\vec{\gamma}^*, \vec{\beta}^*)$  for 40 instances of 16-vertex weighted 3-regular (w3R) graphs, for  $3 \leq p \leq 5$ . Each dashed line connects parameters for one particular graph instance. For each instance and each  $p$ , the BFGS algorithm is used to optimize from  $10^4$  random starting points, and the best parameters are kept as  $(\vec{\gamma}^*, \vec{\beta}^*)$ .

## Appendix B: Details of Heuristic Optimization Strategies

In the main text, we have proposed a class of heuristic strategies called  $\text{FOURIER}[q, R]$  for optimizing QAOA, and focused on application of the strategy where we set  $q = p$  and  $R = 10$ . In our numerical study, we have also examined other natural strategies based on the parameter pattern that we observe. One particular such strategy uses linear interpolation of optimal parameters at lower level QAOA to generate good starting points for higher levels; we call this strategy INTERP. Both INTERP and FOURIER strategies work remarkably well for all the instances we have examined. We have chosen to focus on FOURIER in the main text due to the slight edge in its performance in finding better optima when random perturbations are introduced. We now explain how these strategies work in details, and compare their performances.

### 1. Interpolation-based strategy

In an optimization strategy that we call INTERP, we use linear interpolation to produce a good starting point for optimizing QAOA as one iteratively increases the level  $p$ . This is based on the observation that the shape of parameters  $(\vec{\gamma}_{(p+1)}^*, \vec{\beta}_{(p+1)}^*)$  closely resembles that of  $(\vec{\gamma}_{(p)}^*, \vec{\beta}_{(p)}^*)$ .

The strategy works as follows: For a given instance, we iteratively optimize QAOA starting from  $p = 1$ , and increment  $p$  after obtaining a local optimum  $(\vec{\gamma}_{(p)}^L, \vec{\beta}_{(p)}^L)$ . In order to optimize parameters for level  $p+1$ , we take the optimized parameters from level  $p$  and produce starting points  $(\vec{\gamma}_{(p+1)}^0, \vec{\beta}_{(p+1)}^0)$  according to:

$$[\vec{\gamma}_{(p+1)}^0]_i = \frac{i-1}{p} [\vec{\gamma}_{(p)}^L]_{i-1} + \frac{p-i+1}{p} [\vec{\gamma}_{(p)}^L]_i \quad (\text{B1})$$

for  $i = 1, 2, \dots, p+1$ . Here, we denote  $[\vec{\gamma}]_i \equiv \gamma_i$  as the  $i$ -th element of the parameter vector  $\vec{\gamma}$ , and  $[\vec{\gamma}_{(p)}^L]_0 \equiv [\vec{\gamma}_{(p)}^L]_{p+1} \equiv 0$ . The expression for  $\vec{\beta}_{(p+1)}^0$  is the same as above after swapping  $\gamma \leftrightarrow \beta$ . Starting from  $(\vec{\gamma}_{(p+1)}^0, \vec{\beta}_{(p+1)}^0)$ , we then perform the BFGS optimization routine to obtain a local optimum  $(\vec{\gamma}_{(p+1)}^L, \vec{\beta}_{(p+1)}^L)$  for the  $(p+1)$ -level QAOA. Finally, we increment  $p$  by one and repeat the same process until a target level is reached.

### 2. Details of $\text{FOURIER}[q, R]$ strategy

We now provide the details of our second, main heuristic strategy for optimizing QAOA that we call  $\text{FOURIER}[q, R]$ . As explained in Sec. III B,  $q$  denotes the maximum frequency component we allow in the parameters  $(\vec{u}, \vec{v})$ . When we set  $q = p$ , we denote the strategy

as  $\text{FOURIER}[\infty, R]$ , since  $q$  grows unbounded with  $p$ .

In the basic  $\text{FOURIER}[\infty, 0]$  variant of this strategy, we generate a good starting point for level  $p+1$  by adding a higher frequency component, initialized at zero amplitude, to the optimum at level  $p$ . More concretely, we take parameters from a local optimum  $(\vec{u}_{(p)}^L, \vec{v}_{(p)}^L) \in \mathbb{R}^{2p}$  at level  $p$ , and generate a starting point  $(\vec{u}_{(p+1)}^0, \vec{v}_{(p+1)}^0) \in \mathbb{R}^{2(p+1)}$  according to

$$\vec{u}_{(p+1)}^0 = (\vec{u}_{(p)}^L, 0), \quad \vec{v}_{(p+1)}^0 = (\vec{v}_{(p)}^L, 0). \quad (\text{B2})$$

Using  $(\vec{u}_{(p+1)}^0, \vec{v}_{(p+1)}^0)$  as a starting point, we perform BFGS optimization routine to obtain a local optimum  $(\vec{u}_{(p+1)}^L, \vec{v}_{(p+1)}^L)$  for the level  $p+1$ .

We also consider an improved variant of the strategy,  $\text{FOURIER}[\infty, R > 0]$ , which is sketched alongside the  $R = 0$  variant in Fig. 10. This is motivated by our observation that the basic  $\text{FOURIER}[\infty, 0]$  strategy can sometimes get stuck at a sub-optimal local optimum, whereas perturbing its starting point can improve the performance of QAOA. Here, in addition to optimizing according to the basic strategy, we optimize  $(p+1)$ -level QAOA from  $R+1$  extra starting points,  $R$  of which are generated by adding random perturbations to the best of all local optima  $(\vec{u}_{(p)}^B, \vec{v}_{(p)}^B)$  found at level  $p$ . Specif-

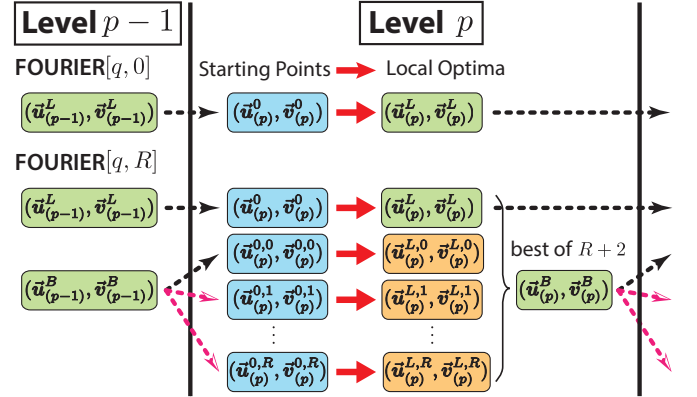


FIG. 10. Schematics of the two variants of  $\text{FOURIER}[q, R]$  heuristic strategy for optimizing QAOA, when  $R = 0$  and  $R > 0$ . Optimal parameters (green) at level  $p-1$  are used to generate good starting points (blue) for optimizing at level  $p$ ; the same process is repeated to optimize for  $p+1$ . When generating starting points, black dashed arrows indicate appending a higher frequency component [Eq. (B2)], and pink dashed arrows correspond to adding random perturbations [Eq. (B3)]. In the  $R > 0$  variant, two local optima (green) are kept in parallel at each level  $p$  for generating good starting points:  $(\vec{u}_{(p)}^L, \vec{v}_{(p)}^L)$  is the same optimum obtained from  $\text{FOURIER}[q, 0]$  strategy, and  $(\vec{u}_{(p)}^B, \vec{v}_{(p)}^B)$  is the best of  $R+2$  local optima,  $R$  of which are obtained from perturbed starting points. We find that keeping the  $(\vec{u}_{(p)}^L, \vec{v}_{(p)}^L)$  optimum improves the stability of the heuristic, as random perturbations can sometimes lead to erratic and non-smooth optimal parameters.

ically, for each instance at  $(p+1)$ -level QAOA, and for  $r = 0, 1, \dots, R$ , we optimize starting from

$$\begin{aligned}\vec{u}_{(p+1)}^{0,r} &= \begin{cases} (\vec{u}_{(p)}^B, 0), & r = 0 \\ (\vec{u}_{(p)}^B + \alpha \vec{u}_{(p)}^{P,r}, 0), & 1 \leq r \leq R \end{cases} \\ \vec{v}_{(p+1)}^{0,r} &= \begin{cases} (\vec{v}_{(p)}^B, 0), & r = 0 \\ (\vec{v}_{(p)}^B + \alpha \vec{v}_{(p)}^{P,r}, 0), & 1 \leq r \leq R \end{cases}\end{aligned}\quad (\text{B3})$$

where  $\vec{u}_{(p)}^{P,r}$  and  $\vec{v}_{(p)}^{P,r}$  contain random numbers drawn from normal distributions with mean 0 and variance given by  $\vec{u}_{(p)}^B$  and  $\vec{v}_{(p)}^B$ :

$$\begin{aligned}[\vec{u}_{(p)}^{P,r}]_k &\sim \text{Normal}\left(0, [\vec{u}_{(p)}^B]_k^2\right), \\ [\vec{v}_{(p)}^{P,r}]_k &\sim \text{Normal}\left(0, [\vec{v}_{(p)}^B]_k^2\right).\end{aligned}\quad (\text{B4})$$

There is a free parameter  $\alpha$  corresponding to the strength of the perturbation. Based on our experience from trial and error, setting  $\alpha = 0.6$  has consistently yielded good results. This choice of  $\alpha$  is assumed in this paper unless otherwise stated.

We remark that the INTERP strategy can also get stuck in a local optimum, but we find that adding perturbations to INTERP does not work as well as to FOURIER. We attribute this to the fact that the optimal parameters are smooth, and adding perturbations in the  $(\vec{u}, \vec{v})$ -space modify  $(\vec{\gamma}, \vec{\beta})$  in a correlated way, which could enable the optimization to escape local optima more easily. Hence, we consider here FOURIER with perturbations, but not INTERP.

Finally, we also consider variants of the FOURIER strategy where the number of frequency components  $q$  is fixed. These variants are the same as aforementioned strategies where  $q = p$ , except we truncated all  $\vec{u}$  and  $\vec{v}$  parameters at the first  $q$  components. For example, when optimizing QAOA at level  $p \geq q$  with the FOURIER $[q, 0]$  strategy, we stop adding higher frequency components and use the starting point  $\vec{u}_{(p+1)}^0 = \vec{u}_{(p)}^L \in \mathbb{R}^q$ .

### 3. Comparison between heuristics

We now examine the difference in the performance among the various heuristic strategies we proposed. For our example instance in Fig. 11, we note that INTERP and FOURIER $[\infty, 0]$  strategies have essentially identical performance (except for small variations barely visible at large  $p$ ). This is expected since both strategies generate starting points for optimizing level  $p+1$  based on smooth deformation of the optimum at level  $p$ . Furthermore, the FOURIER $[\infty, 10]$  strategy outperforms INTERP and FOURIER $[\infty, 0]$  beginning at level  $p \gtrsim 20$ . Interestingly, even when restricting the number of QAOA parameters to  $2q = 10$ , the FOURIER $[5, 10]$  strategy closely matches the performance of other heuristics at low  $p$  and beats

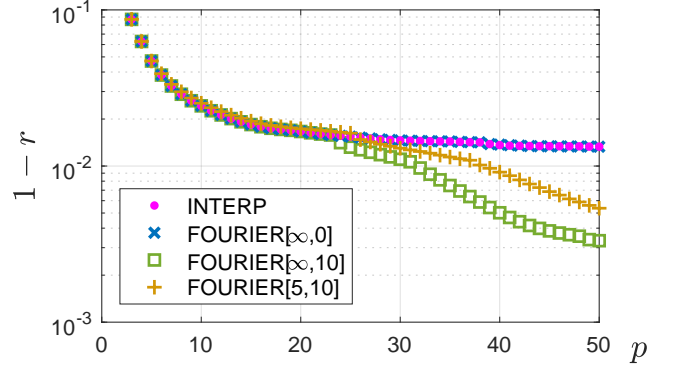


FIG. 11. Comparison between our various heuristics for optimization on an example instance of 14-vertex w3R graph. This is the same example shown in Fig. 6(b).

the  $R = 0$  heuristic at large  $p$ . This suggests that the optimal QAOA parameters may in fact live in a small-dimensional manifold. Therefore, optimization for intermediate  $p$ -level QAOA can be dramatically simplified by using our new parameterization  $(\vec{u}, \vec{v})$ .

### Appendix C: Example graph instance and time-to-solution

In Sec. V B, we focused on a representative graph instance where the adiabatic minimum gap is small [Fig. 6(b)]. The low energy spectrum for the graph along the QA path can be seen in Fig. 12(a). We remark that only eigenstates that are invariant under the parity operator  $\mathcal{P} = \prod_{i=1}^N \sigma_i^x$  are shown, since the Hamiltonian  $H_{\text{QA}}(s)$  commutes with  $\mathcal{P}$  and the initial state is  $\mathcal{P}$ -invariant:  $\mathcal{P}|\psi(0)\rangle = |\psi(0)\rangle$ .

Fig. 12(b) and Fig. 12(c) illustrate TTS<sub>QA</sub> and TTS<sub>QAOA</sub> for the same graph. For QA, one can see that non-adiabatic evolution with  $T \approx 20$  yields orders of magnitude shorter TTS than the adiabatic evolution. We also see that TTS in the adiabatic limit is independent of the annealing time  $T$ , following the Landau-Zener formula  $p_{\text{GS}} = 1 - \exp(-cT\Delta_{\min}^2)$ . For QAOA, we use our FOURIER $[\infty, 10]$  heuristic strategy to perform the numerical simulation up to  $p_{\text{max}} = 50$ , and compute TTS<sub>QAOA</sub>( $p$ ) and TTS<sub>QAOA</sub><sup>opt</sup> (up to  $p \leq p_{\text{max}}$ ). For this particular graph, we note that although TTS<sub>QAOA</sub><sup>opt</sup> occurs at  $p = 49$ , in practice it may be better to run QAOA at  $p = 4$  or  $p = 5$  due to optimization overhead and error accumulation at deeper circuit depths. The apparent discontinuous jump in TTS<sub>QAOA</sub> is due to the corresponding jump in  $p_{\text{GS}}(p)$ , which can be explained by two reasons: first, our heuristic strategy is not guaranteed to find the global optimum, and random perturbations may help the algorithm escape a local optimum, resulting in a jump in ground state population; second, even when the global optimum is found for all level  $p$ , there can still be discon-

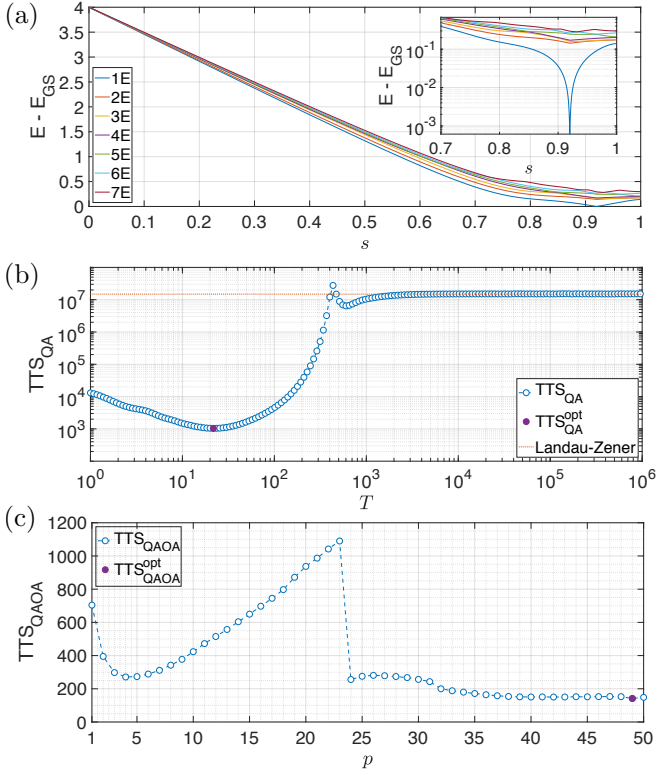


FIG. 12. (a) Energy spectrum of low excited states (measured from the ground state energy  $E_{GS}$ ) along the annealing path for the graph instance given in Fig. 6(b). Only states that can couple to the ground state are shown, i.e., states that are invariant under the parity operator  $\mathcal{P} = \prod_{i=1}^N \sigma_i^x$ . The inset shows the energy gap from the ground state in logarithmic scale. (b) Time-to-solution for the linear-ramp quantum annealing protocol,  $TTS_{QA}$ , for the same graph instance. TTS in the long time limit follows a line predicted by the Landau-Zener formula, which is independent of the annealing time  $T$ . (c) TTS for QAOA at each iteration depth  $p$ .

tinuities in  $p_{GS}$ , since the objective function of QAOA is energy instead of ground state population.

#### Appendix D: Effective few-level understanding of the diabatic bump

In this Appendix, we elucidate the mechanism of the diabatic bump observed in Fig. 6(c) via an effective few-level dynamics. To study the intermediate dynamics during quantum annealing, we can work in the basis of instantaneous eigenstates  $|\epsilon_l(t)\rangle$ , where

$$H_{QA}(t)|\epsilon_l(t)\rangle = \epsilon_l(t)|\epsilon_l(t)\rangle. \quad (D1)$$

Expanding the time-evolved state in this basis as  $|\psi(t)\rangle = \sum_l a_l(t)|\epsilon_l(t)\rangle$ , the Schrodinger equation can be written

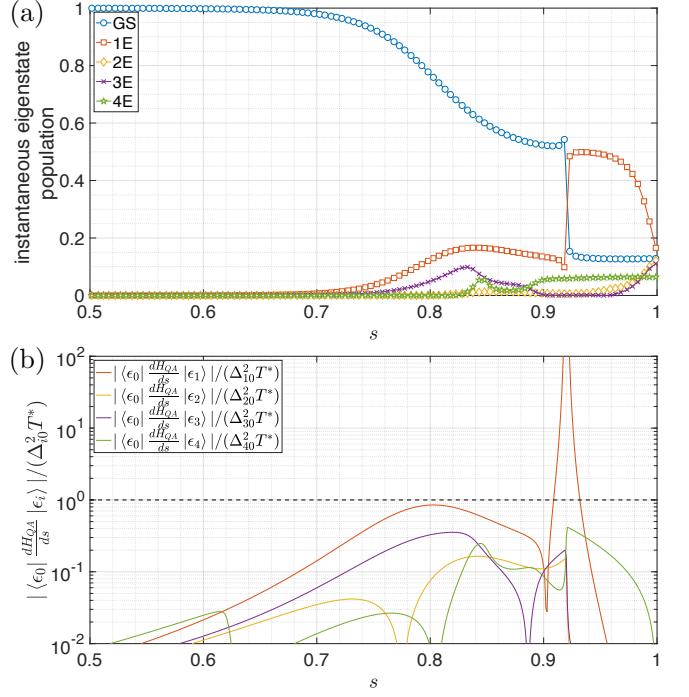


FIG. 13. (a) Instantaneous eigenstate populations along the linear-ramp quantum annealing path given by Eq. (10) for the example graph in Fig. 6(b). The annealing time is chosen to be  $T = T^* = 40$ , which corresponds to the time where the diabatic bump occurs in Fig. 6(c). (b) Coupling between the instantaneous ground states and the first few excited states. The plotted quantities measure the degree of adiabaticity [as explained in Eq. (D5)].

as

$$i \sum_l (\dot{a}_l |\epsilon_l\rangle + a_l |\dot{\epsilon}_l\rangle) = \sum_l \epsilon_l a_l |\epsilon_l\rangle, \quad (D2)$$

where  $\hbar = 1$  and the time dependence in the notations is dropped for convenience. Multiplying the equation by  $|\epsilon_k\rangle$ , the Schrodinger equation becomes

$$i \dot{a}_k = \epsilon_k a_k - i \sum_{l \neq k} a_l \langle \epsilon_k | \dot{\epsilon}_l \rangle, \quad (D3)$$

where  $\langle \epsilon_k | \dot{\epsilon}_k \rangle = 0$  is taken by absorbing the phase into the eigenvector  $|\epsilon_k\rangle$ . Written in a matrix form, we have

$$i \begin{pmatrix} \dot{a}_0 \\ \dot{a}_1 \\ \dot{a}_2 \\ \vdots \end{pmatrix} = \begin{pmatrix} 0 & -i\langle \epsilon_0 | \dot{\epsilon}_1 \rangle & -i\langle \epsilon_0 | \dot{\epsilon}_2 \rangle & \cdots \\ -i\langle \epsilon_1 | \dot{\epsilon}_0 \rangle & \Delta_{10} & -i\langle \epsilon_1 | \dot{\epsilon}_2 \rangle & \cdots \\ -i\langle \epsilon_2 | \dot{\epsilon}_0 \rangle & -i\langle \epsilon_2 | \dot{\epsilon}_1 \rangle & \Delta_{20} & \cdots \\ \vdots & \vdots & \vdots & \ddots \end{pmatrix} \begin{pmatrix} a_0 \\ a_1 \\ a_2 \\ \vdots \end{pmatrix}, \quad (D4)$$

where we take the ground state energy  $\epsilon_0 = 0$  (by absorbing it into the phase of the coefficients) and  $\Delta_{i0} = \epsilon_i - \epsilon_0$  is the instantaneous energy gap from the  $i$ th excited state to the ground state. The time evolution starts from the

initial ground state with  $a_0 = 1$  and  $a_i = 0$  for  $i \neq 0$ , and the adiabatic condition to prevent coupling to excited states is

$$\frac{|\langle \epsilon_0 | \dot{\epsilon}_i \rangle|}{\Delta_{i0}} = \frac{\left| \langle \epsilon_0 | \frac{dH_{\text{QA}}}{dt} | \epsilon_i \rangle \right|}{\Delta_{i0}^2} = \frac{\left| \langle \epsilon_0 | \frac{dH_{\text{QA}}}{ds} | \epsilon_i \rangle \right|}{\Delta_{i0}^2 T} \ll 1. \quad (\text{D5})$$

The first equality can be derived from Eq. (D1). This produces the standard adiabatic condition  $T = O(1/\Delta_{\min}^2)$ . As we discussed in section VB, the minimum gap for some graphs can be exceedingly small, so the adiabatic limit is not practical. However, it may be possible to choose an appropriate run time  $T$ , which breaks adiabaticity, but is long enough such that only few excited states are effectively involved in the dynamics. This is the regime where the diabatic bump operates and one can understand the dynamics by truncating Eq. (D4) to the first few basis states.

As an example, we plot in Fig. 13(a) the instantaneous eigenstate populations of the first few states. It is simulated with the full Hilbert space, but effectively the same dynamics will be generated if the simulation is restricted to the first few basis states in Eq. (D4). Fig. 13(b) shows the strength of the couplings between the instantaneous ground state and the low excited states. By comparing Fig. 13(a) and Fig. 13(b), one can see that  $T = T^* = 40$  allows the time evolution to break the adiabatic condition before the anticrossing: population leaks to the first excited state, which becomes the ground state after the anticrossing. Thus, the time scale of  $T^*$  for the diabatic bump represents a delicate balance between allowing population to leak out of the ground state and suppressing excessive population leakage, which explains why it happens at a certain range of time scale.

## Appendix E: Details of Simulation with Measurement Projection Noise

When running QAOA on actual quantum devices, the objective function is evaluated by averaging over many measurement outcomes, and consequently its precision is limited by the so-called measurement projection noise from quantum fluctuations. We account for this effect by performing full Monte-Carlo simulations of actual measurements, where the simulated quantum processor only outputs approximate values of the objective function obtained by averaging  $M$  measurements:

$$\bar{F}_{p,M} = \frac{1}{M} \sum_{i=1}^M C(\mathbf{z}_{p,i}), \quad (\text{E1})$$

where  $\mathbf{z}_{p,i}$  is a random variable corresponding to the  $i$ th measurement outcome obtained by measuring  $|\psi_p(\vec{\gamma}, \vec{\beta})\rangle$  in the computational basis, and  $C(\mathbf{z})$  is the classical objective function. Note when  $M \rightarrow \infty$ , we obtain  $\bar{F}_{p,M} \rightarrow F_p = \langle \psi_p(\vec{\gamma}, \vec{\beta}) | H_C | \psi_p(\vec{\gamma}, \vec{\beta}) \rangle$ . In the simula-

tion, we achieve finite precision  $|\bar{F}_{p,M} - F_p| \lesssim \xi$  by sampling measurements until the cumulative standard error of the mean falls below the target precision level  $\xi$ . In other words, for each evaluation of  $F_p$  requested by the classical optimizer, the number of measurements  $M$  performed is set by the following criterion:

$$\sqrt{\frac{1}{M(M-1)} \sum_{i=1}^M [C(\mathbf{z}_{p,i}) - \bar{F}_{p,M}]^2} \leq \xi. \quad (\text{E2})$$

Roughly, we expect  $M \approx \text{Var}(F_p)/\xi^2$ . To address issues with finite sample sizes, we also require that at least 10 measurements be performed ( $M \geq 10$ ) for each objective function evaluation.

We now provide some details on the classical optimization algorithm used to optimize QAOA parameters. Generally, classical optimization algorithms iteratively uses information from some given parameter point  $(\vec{\gamma}, \vec{\beta})$  to find a new parameter point  $(\vec{\gamma}', \vec{\beta}')$  that hopefully produces a larger value of the objective function  $F_p(\vec{\gamma}', \vec{\beta}') \geq F_p(\vec{\gamma}, \vec{\beta})$ . In order for the algorithm to terminate, we need to set some stopping criteria. Here, we specify two: First, we set an objective function tolerance  $\epsilon$ , such that if the change in objective function  $|\bar{F}_{p,M'}(\vec{\gamma}', \vec{\beta}') - \bar{F}_{p,M}(\vec{\gamma}, \vec{\beta})| \leq \epsilon$ , the algorithm terminates. We also set a step-tolerance  $\delta$ , so that the algorithm terminates if the new parameter point is very close to the previous one  $|\vec{\gamma}' - \vec{\gamma}|^2 + |\vec{\beta}' - \vec{\beta}|^2 \leq \delta^2$ . For gradient-based optimization algorithms such as BFGS, we also use  $\delta$  as the increment size for estimating gradients via the finite-difference method:  $\partial F_p / \partial \gamma_i \simeq [\bar{F}_{p,M'}(\gamma_i + \delta) - \bar{F}_{p,M}(\gamma_i)] / \delta$ . In our simulations, we use the BFGS algorithm implemented as `fminunc` in the standard library of MATLAB R2017b.

Using the approach described above, we simulate experiments of optimizing QAOA with measurement projection noise for a few example instances, with various choices of precision parameters  $(\epsilon, \xi, \delta)$  and starting points. For the representative instance studied in Fig. 7, we set  $\epsilon = 0.1$ ,  $\xi = 0.05$ , and  $\delta = 0.01$ . In each run of the simulated experiment, we start with QAOA of level either  $p = 1$  or  $p = 5$ , and optimize increasing levels of QAOA using our FOURIER $[\infty, 0]$  heuristic strategy. The starting point of QAOA optimization is either randomly selected (when starting at  $p = 1$ ) or chosen based on an educated guess using optimal parameters from small-sized instances (at  $p = 1$  and  $p = 5$ ). Specifically, the educatedly guessed starting points we use are  $(\vec{u}^0, \vec{v}^0) = (1.4849, 0.5409)$  at level  $p = 1$ , and

$$\vec{u}^0 = (1.9212, 0.2891, 0.1601, 0.0564, 0.0292), \quad (\text{E3})$$

$$\vec{v}^0 = (0.6055, -0.0178, 0.0431, -0.0061, 0.0141) \quad (\text{E4})$$

at level  $p = 5$ . For each such run, we keep track of the history of all the measurements, so that the largest cut  $\text{Cut}_i$  found after the  $i$ -th measurement can be calculated. We repeat each experiment for 500 times with

different pseudo-random number generation seeds, and average over their histories.

## Appendix F: Techniques to speed up numerical simulation

In this Appendix, we discuss a number of techniques we exploited to speed up the numerical simulation for both QAOA and QA.

First, we make use of the symmetries present in the Hamiltonian. For general graphs, the only symmetry operator that commutes with both  $H_C$  and  $H_B$  is the parity operator  $\mathcal{P} = \prod_{i=1}^N \sigma_i^x$ :  $[H_C, \mathcal{P}] = 0, [H_B, \mathcal{P}] = 0$ , and so does  $[H_{\text{QA}}(s), \mathcal{P}] = 0$ , where  $H_{\text{QA}}(s)$  is the quantum annealing Hamiltonian in Eq. (10). The parity operator has two eigenvalues, +1 and -1, each with half of the entire Hilbert space. The initial state for both QAOA and QA is in the positive sector, i.e.,  $\mathcal{P}|+\rangle^{\otimes N} = |+\rangle^{\otimes N}$ . Thus, any dynamics remain in the positive parity sector. We can rewrite  $H_C$  and  $H_B$  in the basis of the eigenvectors of  $\mathcal{P}$ , and reduce the Hilbert space from  $2^N$  to  $2^{N-1}$  by working in the positive parity sector.

For QA, dynamics involving the time-dependent Hamiltonian can be simulated by dividing the total simulation time  $T$  into sufficiently small discrete time  $\tau$  and implement each time step sequentially. At each small step, one can evolve the state without forming the full evolution operator [67], either using Krylov subspace projection method [68] or a truncated Taylor series approx-

imation [69]. In our simulation, we used a scaling and squaring method with a truncated Taylor series approximation [69] as it appears to run slightly faster than the Krylov subspace method for small time steps.

For QAOA, the dynamics can be implemented in a more efficient way due to the special form of the operators  $H_C$  and  $H_B$ . We work in the standard  $\sigma_z$  basis. Thus,  $H_C = \sum_{\langle i,j \rangle} \frac{w_{ij}}{2} (\mathbb{1} - \sigma_i^z \sigma_j^z)$  can be written as a diagonal matrix and the action of  $e^{-i\gamma H_C}$  can be implemented as vector operations. For  $H_B$ , the time evolution operator can be simplified as

$$e^{-i\beta H_B} = \prod_{j=1}^N e^{-i\beta \sigma_j^x} = \prod_{j=1}^N (\mathbb{1} \cos \beta - i \sigma_j^x \sin \beta). \quad (\text{F1})$$

Therefore, the action of  $e^{-i\beta H_B}$  can also be implemented as  $N$  sequential vector operations without explicitly forming the sparse matrix  $H_B$ , which both improves simulation speed and saves memory. In addition, in the optimization of variational parameters, we calculated the gradient analytically, instead of using finite-difference methods. Techniques similar to the gradient ascent pulse engineering (GRAPE) method [70] were used, which reduces the cost of computing the gradient from  $O(p^2)$  to  $O(p)$ , for a  $p$ -level QAOA. Lastly, in our FOURIER strategy, we need to calculate the gradient of the objective function with respect to the new parameters  $(\vec{u}, \vec{v})$ . Since  $\vec{\gamma} = A_S \vec{u}$  and  $\vec{\beta} = A_C \vec{v}$  for some matrices  $A_S$  and  $A_C$ , their gradients are also related via  $\nabla_{\vec{u}} = A_S \nabla_{\vec{\gamma}}$  and  $\nabla_{\vec{v}} = A_S \nabla_{\vec{\beta}}$ .